

VAND-TH-99-10

A Tale of Two Hard Pomerons

Arjun Berera* †

Department of Physics and Astronomy, Vanderbilt University, Nashville, TN 37235, U.S.A.

(September 14 , 1999)

Abstract

Two mechanisms are examined for hard double pomeron exchange dijet production, the factorized model of Ingelman-Schlein and the nonfactorized model of lossless jet production which exhibits the Collins-Frankfurt-Strikman mechanism. Comparison between these two mechanisms are made of the total cross section, E_T -spectra, and mean rapidity spectra. For both mechanisms, several specific models are examined with the cuts of CDF, D \emptyset and representative cuts of LHC. The preliminary CDF and D \emptyset data for this process are interpreted in terms of these two mechanisms. The experimental data is suggestive of a dominant component of the factorized Ingelman-Schlein mechanism, although as is discussed there are some inconsistencies.

PACS number(s): 13.85.-t, 12.38.Qk, 13.87.Ce

I. INTRODUCTION

High energy hadron-hadron scattering is deeply rooted in Regge theory. As a phenomenology, Regge theory succeeds in a complete gambit of processes: elastic scattering, inelastic scattering, inclusive elastic diffraction, exclusive elastic diffraction (for a review please see [1,2]). The content of Regge theory is more profound than simply a parametrically well fit model. Through nontrivial analyticity, unitarity and crossing relations, Regge theory is highly predictive. For high energy hadron-hadron scattering, the core of Regge phenomenology is the Pomeron, the vacuum exchange trajectory. By definition, high energy elastic scattering of two hadrons $h_1 h_2 \rightarrow h_1 h_2$ is mediated by the Pomeron, since no quantum numbers apart from angular momentum are exchanged in the process.

*E-mail: ab@ph.ed.ac.uk

†Present address, Department of Physics and Astronomy, University of Edinburgh, Edinburgh EH9 3JZ, United Kingdom

Although by the late 60s, Regge physics could explain more than a coincidental variety of processes, efforts to explain it from a deeper perspective became frustrated. Instead, Bjorken scaling, the Feynman parton model and perturbative QCD (pQCD) became a successful trio for development. With this turn in theoretical interest to parton physics, in the early 70's the era of novel high energy diffractive experiments came to an end for over a decade. During this time, the pQCD parton model achieved proven success in hard processes, i.e. DIS, Drell-Yan, inclusive hadron-hadron scattering. All these hard processes are typified by production of particles with very high transverse momentum relative to the center-of-mass collision axis. The parton model became, and still is, the only unifying concept about hadronic structure that can be confirmed by first principles quantum field theory via perturbative QCD.

Once parton physics was well confirmed in hadron scattering, the idea eventually emerged to test parton ideas in diffractive scattering. This is a natural direction to investigate, since it embraces and deepens the universal prevalence of partons in hadronic structure. The first attempt at this was by the UA4 experiment [3], which examined the process $pp \rightarrow pX$ at $\sqrt{s} = 540$ GeV. Motivated by this experiment, Ingelman and Schlein made the important suggestion¹ of probing the pomeron via hard scattering processes [4]. In their model, diffractive scattering is attributed to the exchange of a pomeron, which operationally is defined as a colorless object with vacuum quantum numbers. Their model treats the pomeron like a real particle and so considers, for example, that a diffractive electron-proton collision is due to an electron-pomeron collision and that a diffractive hadron-hadron collision is due to a proton-pomeron collision for single-sided diffraction and pomeron-pomeron collision for double diffraction. Their suggestion was confirmed by the UA8 experiment [7,8] which reported jet events in $pp \rightarrow pX$ collisions at $\sqrt{s} = 630$ GeV. At about the same time as the UA8, the UA1 was reporting jet events with double rapidity gaps at $\sqrt{s} = 630$ GeV, which had the suggestive features of hard double pomeron exchange [9].

For diffractive hard process, such as the above examples, first comes a question of pure semantics, whether or not to say the diffractive proton "exchanged a pomeron". Only one Pomeron has entitled historical rights to this name, and that is the Pomeron of soft Regge physics [10,11] (also sometimes called the soft Pemeron). Reference to pomeron in any other case exploits this established trademark as a mnemonic for describing some portion of the process in which a strong interaction scattering occurred that involved the exchange of no quantum numbers except angular momentum. In our discussion of diffractive hard scattering, we will adhere to this standard convention but we will use the lower case pomeron in reference to a process in which one or both incoming hadrons diffracts into the final state along with a hard process. On the other hand, the upper case Pomeron will be reserved for the vacuum exchange trajectory of soft Regge physics [10,11]. There is general belief that properties of the Pomeron reflect in the pomeron of diffractive hard scattering, although it is a central research question to identify the specifics. Spacetime arguments generically suggest that hard events are well localized in space and time. Thus it is expected that in a diffractive hard process, the diffractive hadrons undergo effects similar to what they would encounter in a high-energy elastic scattering. As such, diffractive hard physics is expected to involve long-

¹Some other works at around the same time also had similar ideas [5,6]

time, long distance, thus nonperturbative, physics. Nevertheless, that hard processes can occur intermittent to the diffractive scattering indicates that diffractive hadronic physics, via the pomeron, also possesses perturbative properties.

The hard processes constitute a tiny fraction of all processes governed by pomeron exchange. However they are of interest, since many aspects of such processes can be explained from first principles quantum field theory via perturbative QCD. For the most part, pomeron physics in hard diffraction is nonperturbative, since it involves the confining properties of QCD. Until confinement is understood, identifying perturbative aspects to the pomeron provides some fundamental probe to it.

At present, the modest goal of diffractive hard scattering physics is to identify aspects of the pomeron that unify its perturbative behavior described through pQCD with its nonperturbative behavior, which in some limit is believed to be described through Regge physics. Various descriptive modes have emerged to describe the pomeron, e.g. hard, soft, perturbative, nonperturbative, factorizable, nonfactorizable, coherent... This terminology plethora is in best hopes temporary. Its underlying purpose is to assist in describing properties of the pomeron that unambiguously can be confirmed by QCD. Ideally, identifying such properties would mark an advance mutually in verifying QCD as the theory of strong interactions and in determining the role of the pomeron and Pomeron within QCD.

The distinctive difference between QCD and Regge diffractive physics is the presence of color flow in the former. This fact permits a richer spacetime structure to diffractive physics than expected from ordinary Regge physics. The presence of color in QCD implies pomeron exchange in simplest form is a two gluon exchange process [12,13]. Necessarily, the simplest model of the pomeron must involve at least two partons in order to be color singlet. The two-gluon model of the pomeron has been used to explain a variety of soft and hard pomeron characteristics. To achieve hard diffraction's present agenda of revealing perturbative aspects of the pomeron, one seeks signatures in which the soft diffractive event is minimally disturbed yet concurrently in which color flow properties of QCD are exploited in ways that could not be achieved by standard Regge phenomenology. For this, two questions must be addressed. First, what is the diffractive process of choice? Second, what is the most revealing signature?

In principle, the answer to the first question unambiguously is hard double-pomeron-exchange (DPE) processes, due to their authenticity to soft diffraction. In particular, these processes have the naive appearance of an elastic hadron-hadron scattering in which a spacetime localized hard process impinges somewhere in the middle of the collision. This is a little too naive since the partons necessary to initiate the hard event separated color in the hadron beam jets. This should modify the soft interactions between the two beam jets relative to the case of pure elastic scattering. In any case, amongst the diffractive hard processes, the DPE hard process is simpler for two reasons. First, the final state of the two beam jets is well defined, in particular, to be again the two incoming hadrons. Second, such a final state is very clean, since both final state beam jets are well localized color singlets, so can not interact with other spacetime regions. Both these reasons simplify the theoretical description of this process. In contrast, for the other diffractive hard processes, e.g. single-sided diffraction or diffractive excitation, color is separated at the hard event and in one or both final state beam jets. QCD effects are much more complicated since they will occur between all regions in which color has been separated. This further complicates the separation of

effects that clearly can be identified with perturbative QCD versus those with soft diffractive Regge physics.

The second question also has a possible unambiguous answer in the context of factorized versus nonfactorized processes². In spacetime, for a factorized process, the effect of the two incoming particles act independently on the hard event. For diffractive deep inelastic scattering, basic ideas of factorization were outlined and diffractive parton distribution functions were defined in [15,16]³. A proof of factorization for diffractive DIS was given in [17]. For hard diffraction in pure hadronic collisions, Collins, Frankfurt and Strikman (CFS) [19] have demonstrated a counterargument to this picture. The CFS mechanism is a leading twist effect in which all the momentum lost by the diffractive hadrons goes into the hard event. This mechanism was identified earlier by Frankfurt and Strikman [20]. They originally referred to the nonfactorized pomeron of CFS as the coherent pomeron. Subsequently, the UA8 presented results in which up to 30 percent of the dijet events in single-sided diffraction could be associated with the coherent pomeron, which they in turn named the superhard pomeron. With the hindsight of the UA8 experiment and the ideas of CFS, in [15] the CFS mechanism was applied to a toy quantum field theory model of diffractive dijet photoproduction, in which the pomeron was represented by two gluon exchange. This work in turn, in turn, named the nonfactorizing, alias superhard, alias coherent pomeron process as lossless diffractive hard scattering to emphasize the efficient transfer of the pomeron momentum to the hard process.

The two gluon pomeron model has an essential property for any pure hadron initiated reaction, which is a realization of the CFS mechanism. Consider the hard DPE process $h_1 h_2 \rightarrow h_1 h_2 + \text{hard}$. The two gluons exchanged by h_1 are not both obliged to enter the hard event. Instead, one gluon may attach to h_2 . In this case, the two incoming hadrons no longer act independently in inducing the hard event. By definition of hard factorization [14,21], such a process is nonfactorizing. This CFS mechanism has been developed for hard DPE in $p\bar{p}$ collisions⁴ for quark jets in [22] and gluon jets in [23]. The gluon jet process was shown in [23] to dominate the quark jet process by several orders of magnitude.

The purpose of this paper is to examine for the DPE dijet process, general differences between the factorized pomeron model of Ingelman and Schlein, F(IS)DPE [4], and the non-factorized pomeron model of lossless jet production of Berera and Collins [23], N(L)DPE. Our notation specifies in the context of hard factorization whether the process is factorizable, F, or nonfactorizable, N, and in parenthesis gives the particular type of process. The latter specification is necessary since there are several different types of factorizable and nonfactor-

²A general review of factorization in hard scattering is given in [14].

³Closely related to diffractive parton distribution functions is fracture functions [18]

⁴The first nonfactorizing DPE two gluon model was developed before CFS for Higgs [24] and heavy quark [25] production. Although the nonfactorizing mechanism is the same as that of CFS [19] and [15,22,23], these earlier papers did not recognize the full consequences of nonfactorization to the extent done by CFS.

izable processes. Detailed discussions about this point are in [19,15,16,23,17,26,27]. As one example, factorized processes first have a basic distinction between simple hard factorization and the more specific Regge factorization [16]. In particular, the factorized Ingelman-Schlein DPE model also is Regge factorized⁵. For nonfactorization, one example outside of the CFS mechanism is the "flux renormalization" prescription of Goulianos [28], which arises due to a breakdown of the triple-Regge theory for soft diffractive excitation. Also, nonfactorization is found in pre-QCD analysis of diffractive processes [29]. An empirical analysis by Alvero, Collins and Whitmore [30] of the preliminary CDF double diffractive dijet data [31,32] indicates that hard factorization is violated in this process. In fact, their analysis suggests for parton distribution functions that are most consistent over all diffractive processes, the experimental DPE dijet cross section is much less than expected by factorization. On the other hand, the nonfactorizing CFS mechanism should enhance the cross section. Nevertheless, the analysis in [30] does not rule-out experimental realization of the CFS mechanism, since account must be given to all sources of nonfactorization before the overall trends expected from theory can be assessed. For example, another potential source of nonfactorization is absorptive corrections, which are found in Regge models [33] of diffractive scattering. These effects are expected to suppress the cross section.

At this point in this discussion, theoretical limitations are reached, primarily due to a lack of knowledge about long distance QCD. Currently, no systematic approach is available to analyze nonfactorizing effects in diffractive hard scattering. Rather, our approach must be phenomenological and we must look for characteristic behaviors that differentiate the various contributions to the process. The modest goal of this paper is to do that with focus on comparing F(IS)DPE and N(L)DPE. For this, we will calculate the E_T and mean jet rapidity spectra and total cross sections for both processes, with the cuts of CDF, DØ and representative cuts for LHC. The emphasis of this study is to identify qualitative differences that should be expected between the two types of pomeron models.

The paper is organized as follows. Sect. II reviews the kinematics of DPE dijet production and then models are presented for the nonfactorized and factorized processes. The inclusive dijet cross section also is reviewed in Sect. II and will be computed in later sections for comparison purposes. In Sect. III the CDF and DØ cuts for DPE dijet production are reviewed and representative cuts for LHC are presented. In Sect. IV results of our calculations are presented for DPE and inclusive dijet E_T and mean rapidity spectra and total cross sections. Subsect. IV A gives a general presentation of the results, Subsect. IV B examines the results in greater detail and Subsect. IV C compares our results with the preliminary data of CDF and DØ. Finally Sect. V presents our conclusions. Also in Sect. V we discuss limitations of our models and compare with related models.

⁵Hereafter our usage of factorization without further specification always means in the context of hard factorization.

II. MODELS

This section reviews the kinematics of DPE dijet production and the formulas for the F(IS)DPE and N(L)DPE models, based on the presentation in [23].

A. Kinematics

The DPE dijet process examined in this paper is shown in Fig. 1,

$$p + \bar{p} \rightarrow p' + \bar{p}' + 2 \text{ jets.} \quad (1)$$

The proton and antiproton collide at high center of mass energy $s \equiv (P_p + P_{\bar{p}})^2 \rightarrow \infty$, lose tiny fractions $x_{IP/p}$ and $x_{IP/\bar{p}}$ of their respective longitudinal momenta, and acquire transverse momenta \mathbf{Q}_p and $\mathbf{Q}_{\bar{p}}$. (This defines a diffractive regime, and in Regge theory would lead to an expectation of the dominance of double pomeron exchange (DPE)). Using light-cone coordinates $(+, -; \perp)$, the components of momenta of the hadrons in Fig. 1 are

$$\begin{aligned} P_p &= \left(\sqrt{\frac{s}{2}}, \frac{M^2}{\sqrt{2s}}; \mathbf{0} \right) \\ P_{\bar{p}} &= \left(\frac{M^2}{\sqrt{2s}}, \sqrt{\frac{s}{2}}; \mathbf{0} \right) \\ P_{p'} &= \left((1 - x_{IP/p}) \sqrt{\frac{s}{2}}, \frac{(M^2 + \mathbf{Q}_p^2)}{(1 - x_{IP/p})\sqrt{2s}}; \mathbf{Q}_p \right) \\ P_{\bar{p}'} &= \left(\frac{(M^2 + \mathbf{Q}_{\bar{p}}^2)}{(1 - x_{IP/\bar{p}})\sqrt{2s}}, (1 - x_{IP/\bar{p}}) \sqrt{\frac{s}{2}}; \mathbf{Q}_{\bar{p}} \right). \end{aligned} \quad (2)$$

Here we use bold-face type to indicate two-dimensional transverse momentum.

The jets carry large momenta of magnitude E_T in the plane perpendicular to the collision axis with azimuthal angle ϕ . (This defines a hard-scattering regime.) The small transfer of longitudinal momentum to the hard process implies large rapidity gaps between the jets and the two outgoing hadrons. The momentum delivered by the two incoming partons to the hard collision that creates the jets is some portion $x_p, x_{\bar{p}}$ of the longitudinal momentum fractions $x_{IP/p}, x_{IP/\bar{p}}$ respectively, $0 < x_p \leq x_{IP/p}$, $0 < x_{\bar{p}} \leq x_{IP/\bar{p}}$. Thus for the jets, ignoring terms of relative order $\ll 1$, the components of their momenta are

$$\begin{aligned} p_1 &= \left(ax_p \sqrt{\frac{s}{2}}, bx_{\bar{p}} \sqrt{\frac{s}{2}}; E_T \cos \phi, E_T \sin \phi \right) \\ p_2 &= \left(bx_p \sqrt{\frac{s}{2}}, ax_{\bar{p}} \sqrt{\frac{s}{2}}; -E_T \cos \phi, -E_T \sin \phi \right), \end{aligned} \quad (3)$$

where it is convenient to define

$$\begin{aligned} a &\equiv \frac{1 + \sqrt{1 - \kappa}}{2}, \\ b &\equiv 1 - a, \end{aligned} \quad (4)$$

with

$$\kappa \equiv \frac{4E_T^2}{x_p x_{\bar{p}} s}. \quad (5)$$

For later use, define the ratios

$$\beta_p \equiv \frac{x_p}{x_{IP/p}}, \quad \beta_{\bar{p}} \equiv \frac{x_{\bar{p}}}{x_{IP/\bar{p}}}. \quad (6)$$

It is conventional to describe the jet kinematics through the transverse momentum E_T in Eq. (3) and the rapidity variables

$$y_1 \equiv \frac{1}{2} \ln \frac{p_1^+}{p_1^-}, \quad y_2 \equiv \frac{1}{2} \ln \frac{p_2^+}{p_2^-}, \quad (7)$$

which sometimes are expressed as $y_+ \equiv (y_1 + y_2)/2$ and $y_- \equiv y_1 - y_2$. In terms of the jet rapidity variables and E_T , we have

$$\begin{aligned} x_p &= \frac{E_T}{\sqrt{s}} (e^{y_1} + e^{y_2}), \\ x_{\bar{p}} &= \frac{E_T}{\sqrt{s}} (e^{-y_1} + e^{-y_2}), \end{aligned} \quad (8)$$

and

$$\kappa = \frac{1}{\cosh^2(y_-/2)}. \quad (9)$$

B. Factorized (Inglemann-Schlein) DPE - F(IS)DPE

To obtain the expression for the Factorized (Ingleman-Schlein) DPE (F(IS)DPE) dijet differential cross section, first recall the inclusive dijet differential cross section (Fig. 2)

$$\frac{d\sigma_{inclus.}^{dijet}}{dy_1 dy_2 dE_T^2} = \frac{\pi}{s} \sum_{ij} [f_{i/p}(x_p) f_{j/\bar{p}}(x_{\bar{p}}) \hat{\sigma}_{ij}(\hat{s}, \hat{t}, \hat{u}) + f_{j/p}(x_p) f_{i/\bar{p}}(x_{\bar{p}}) \hat{\sigma}_{ij}(\hat{s}, \hat{t}, \hat{u})] / (1 + \delta_{ij}), \quad (10)$$

where s is the CM energy between the two incoming hadrons (here protons), $f_{i/h}(x_h)$, is the inclusive parton distribution functions for parton species i in hadron h , and $x_p, x_{\bar{p}}$ are the parton momentum fractions relative to proton and antiproton respectively, carried by the two partons going into the hard interaction. $\hat{\sigma}_{ij}$ is the parton 2 to 2 cross section for parton species i and j with explicit expressions given in [34].

In the IS picture, they regard the pomeron as a hadronic particle. The pomeron is hypothesized to be created from the incoming proton and carries some momentum fraction $x_{IP/h}$, $h = p, \bar{p}$, of that proton's longitudinal momentum. In DPE hard expressions, one simply thinks of the collision of two pomerons in the same way as any two incoming hadronic particles. As such, the inclusive dijet expression, Eq. (10) above, applies to this case with

two modifications. First s now must be replaced by the appropriate CM energy for the two pomerons, which is precisely $x_{IP/p}x_{IP/\bar{p}}s$, where s here is the CM energy between the two incoming protons. Second a “pomeron flux factor” must be introduced, that expresses the probability to find a pomeron inside the proton.

With these considerations in mind, the expression to F(IS)DPE dijet differential cross section is (Fig. 3)

$$\begin{aligned} \frac{d\sigma_{F(IS)DPE}^{dijet}}{dy_1 dy_2 dE_T^2} &= \int dx_{IP/p} dx_{IP/\bar{p}} f_{IP/p}(x_{IP/p}) f_{IP/\bar{p}}(x_{IP/\bar{p}}) \frac{\pi}{x_{IP/p} x_{IP/\bar{p}} s} \\ &\quad \sum_{ij} [f_{i/IP}(\beta_p) f_{j/IP}(\beta_{\bar{p}}) \hat{\sigma}_{ij}(\hat{s}, \hat{t}, \hat{u}) \\ &\quad + f_{j/IP}(\beta_p) f_{i/IP}(\beta_{\bar{p}}) \hat{\sigma}_{ij}(\hat{s}, \hat{t}, \hat{u})] / (1 + \delta_{ij}). \end{aligned} \quad (11)$$

In this expression $x_p, x_{\bar{p}}$ again are the momentum fractions of the incoming partons relative to the respective protons and β_h are the parton momentum fraction with respect to the pomeron, as defined in Eq. (6). $f_{i/IP}(\beta_h)$ now is the pomeron parton distribution function. $\hat{\sigma}_{ij}$ is the parton 2 to 2 cross section, which is the same as in the above inclusive case Eq. (10). Finally, $f_{IP/h}(x_{IP/h})$ is the “pomeron flux factor”. In our work, we will use the pomeron flux factor of Donnachie and Landshoff⁶ [35],

$$f_{IP/p}^{DL}(x_{IP}) = f_{IP/\bar{p}}^{DL}(x_{IP}) = \int_{-1}^0 dt \frac{9\beta_0^2}{4\pi^2} \left[\frac{4m_p^2 - 2.8t}{4m_p^2 - t} \left(\frac{1}{1 - t/0.7} \right)^2 \right]^2 x_{IP}^{1-2\alpha(t)}, \quad (12)$$

where $m_p \approx 0.938 \text{ GeV}$ is the proton mass, $\beta_0 \approx 1.8 \text{ GeV}^{-1}$ is the pomeron-quark coupling and $\alpha(t) = \alpha_{IP} + 0.25t$ is the pomeron trajectory. α_{IP} is known as the pomeron intercept which for the soft Pomeron is $\alpha_{IP} \approx 1.08$ [38]. For the fits by Alvero, Collins, Terron and Whitmore (hereafter ACTW) [36] to diffractive deep inelastic and diffractive photoproduction of jets, which are used in this paper, α_{IP} was a free parameter that was fit to data and found to be $\alpha_{IP} \approx 1.14$.

The parton densities used here are the five models fit by ACTW [36]. This covers a very general set of possibilities. Retaining their notation, the models will be denoted as ACTW A, B, C, D, and SG. The precise description of these models can be found in Sect. IID. of their paper. In brief, the models A-D use conventional shapes for the initial distributions. Model A represents a conventional hard quark parametrization, B has in addition to A an initial gluon distribution, C has in addition to A a soft quark distribution, and D has both additions to A. The final fit has a gluon distribution that is peaked near $\beta = 1$. This form was motivated by the fit obtained by the H1 collaboration. In [36], they refer to it also as the “super-hard gluon”.

⁶There is another commonly used pomeron flux factor which is of Ingelman and Schlein [4]. This differs from the DL flux factor primarily in its normalization. However a change in the normalization factor completely is compensated for by changing the parton densities by an inverse factor. Thus the parton densities are obtained, for example in [36] for a set of data without any *a priori* expectations as to their normalization.

C. Nonfactorized (Lossless) DPE - N(L)DPE

Our expression for the N(L)DPE dijet cross section is based on the toy quantum field theory model in [23] which in effect is the model of Low-Nussinov-Gunion-Soper [12,13]. The N(L)DPE dijet cross section expression obtained here extends from [23] to account for the one-loop Sudakov suppression factor. We presented preliminary results with Sudakov suppression in [39]. Our treatment of Sudakov suppression is the same as by Martin, Ryskin, and Khoze⁷ [40]. In fact, at one-loop order the nonabelian expression required here is the same as the abelian expression of Sudakov [41] which in the context of hard scattering was obtained earlier by Collins [42]. The only difference is, the abelian expression must be multiplied by an overall group theory factor to account for the additional color degrees in the nonabelian case.

For the N(L)DPE model in Fig. 4b, $x_{IP/p}$ and $x_{IP/\bar{p}}$ again are the longitudinal momentum fractions lost by proton and antiproton respectively. In difference to the F(IS)DPE case, the momentum fractions for the incoming partons to the hard process are equal to those lost by the protons, $x_p = x_{IP/p}$ and $x_{\bar{p}} = x_{IP/\bar{p}}$ or equivalently $\beta_p = \beta_{\bar{p}} = 1$. Qualitatively this means all the momentum lost by the diffractive protons is transferred into the hard process. This kinematics is similar to the superhard component reported for the case of single-sided diffractive dijet production by the UA8 [8].

Our expression for the N(L)DPE dijet differential cross section is

$$\frac{d\sigma_{N(L)DPE}^{dijet}}{dE_T^2 dy_- dy_+} = \int d^2 \mathbf{Q}_p d^2 \mathbf{Q}_{\bar{p}} \frac{|\bar{\mathcal{M}}|^2 \kappa^2}{2^{16} \pi^7 E_T^4}, \quad (13)$$

where

$$\bar{\mathcal{M}} = -(-i) \int \frac{d^2 \mathbf{k}}{(2\pi)^2} \hat{g}_p(\mathbf{k}, -\mathbf{Q}_p) \hat{g}_{\bar{p}}(\mathbf{k}, \mathbf{Q}_{\bar{p}}) \epsilon_i(\mathbf{k} - \mathbf{Q}_p) \epsilon_j(-\mathbf{k} - \mathbf{Q}_{\bar{p}}) \mathcal{A}(i, j; f) F_S(\mathbf{k}^2, E_T^2) \quad (14)$$

Here, the “polarization” vectors are defined as

$$\epsilon_i(\mathbf{k}) = \frac{\mathbf{k}_i}{\sqrt{\mathbf{k}^2}}, \quad (15)$$

$\hat{g}_h(\mathbf{k}, \mathbf{Q})$ are hadronic form factors with the explicit expressions of our model in Eqs. (10) - (12) of [23], and $\mathcal{A}(i, j; f)$ is the hard amplitude. Two hard subprocesses are possible, $g_1' g_2' \rightarrow g_1 g_2$ and $g_1' g_2' \rightarrow q_1 \bar{q}_2$. The calculations in [22,23] showed that the latter process gives zero contribution to the N(L)DPE dijet cross section when the final state transverse

⁷In [40] two types of double diffractive dijet expressions are given, which they call exclusive and inclusive. Both these expressions are nonfactorizing processes of the CFS type, with the exclusive case the same as our N(L)DPE model. Their inclusive case implements the same two gluon nonfactorizing mechanism as their exclusive case. The difference is, for the inclusive case the incoming protons can diffract to any final state, provided there are rapidity gaps between these final states and the hard process. This process is not relevant to this paper.

momentum of the two diffractive hadrons is zero. This should suppress quark jet production relative to gluon jet production. In [23] this expectation was explicitly confirmed. Thus only the $g_1'g_2' \rightarrow g_1g_2$ hard process is relevant for N(L)DPE production.. The explicit expressions for $\mathcal{A}(i, j; f)$ for this process are given in Appendix A of [23]. The Sudakov suppression factor is $F_S(\mathbf{k}^2, E_T^2)$, which at one-loop order is [42,40]

$$F_S(\mathbf{k}^2, E_T^2) = \exp \left[-S(\mathbf{k}^2, E_T^2) \right], \quad (16)$$

where

$$S(\mathbf{k}^2, E_T^2) = \frac{3\alpha_S(E_T^2)}{4\pi} \ln^2 \left[\frac{E_T^2}{4(\mathbf{k}^2 + \mu^2)} \right] \quad (17)$$

where μ ($\lesssim 1\text{GeV}$) is a low energy cutoff scale.

The amplitude $\overline{\mathcal{M}}$ in Eq. (14) is fixed up to an overall normalization which implicitly is specified through the hadronic form factors g_h . Based on the same quantum field theory model, an expression for the hadron-hadron elastic scattering amplitude can be determined and that expression involves the same hadronic form factors g_h . In fact this expression for the elastic scattering amplitude essentially is the one of Low-Nussinov [12] and Gunion-Soper [13]. Thus the free parameter in our N(L)DPE model that fixes the overall normalization of $\overline{\mathcal{M}}$ is chosen to yield the experimental value of the $p\bar{p}$ forward elastic cross section. The details of this procedure are given in [23].

III. EXPERIMENTAL CUTS

This section reviews details about the CDF and DØ experiments that are relevant to the DPE dijet process. In particular, we state the cuts we will use to represent the CDF and DØ DPE dijet experiments. Also, cuts are given that are representative cases for DPE dijets at LHC.

CDF has presented results on double diffractive dijet production [31,32,43,44] at $\sqrt{s} = 1800\text{GeV}$ with transverse jet energies $E_T > 7\text{GeV}$. The experiment has one Roman pot on the $-$ rapidity side, which detects the diffractive hadron, here \bar{p} , going in this direction with the cuts $0.04 < x_{IP/\bar{p}} < 0.095$. On the $+$ rapidity side, there is no Roman pot, only a rapidity gap requirement. Thus, in principle, there is no specified cuts on the outgoing diffractive hadron, here p , that goes in the $+$ rapidity side. However, based on the rapidity gap length on this side, they obtain the estimate $0.015 < x_{IP/p} < 0.035$. The experiment places no explicit cuts on the dijet rapidity region. In our calculations, as our cuts, we will use the entire central detector region $-4.2 < y_1, y_2 < 2.0$.

The CDF double diffractive dijet experiment has three shortcomings in its interpretation as the DPE dijet process. First, the lack of a Roman pot on the $+$ rapidity side to detect the proton is a primary source of ambiguity in differentiating rapidity gap events that involve diffractive excitation of the proton versus pomeron exchange. Second, a heuristic guide for pomeron exchange is that in the diffractive event $x_{IP/p, \bar{p}} < 0.05$. Above this limit other Regge exchanges may be important or the interpretation as a diffractive process altogether may be questioned. Based on this guide, the CDF Roman pot cuts on the diffractive

antiproton, $0.04 < x_{IP/\bar{p}} < 0.095$, exceed the optimal region for interpretation as pomeron exchange. Third, CDF does not implement on-line jet triggering. Instead, they collect a sample of events that have a \bar{p} track in the Roman pot and a rapidity gap in the +rapidity, p , side. From these events, they separate those cases in which there are two jets in the central region with $E_T > 7\text{GeV}$ and discard the remaining data. Since generally jets are difficult objects to create and the central region typically is soft, most of the collected data is discarded. Furthermore, $E_T > 7\text{GeV}$ is a relatively low transverse jet momentum requirement for Tevatron jets and at this level jets are fairly cloudy objects that may be difficult to reconstruct and measure precisely.

$D\emptyset$ has been examining double diffractive dijet production at two center-of-mass energies $\sqrt{s} = 630\text{GeV}$ and 1800GeV [45–48]. Hereafter these two cases will be referred to respectively as $D\emptyset 630$ and $D\emptyset 1800$. At present, the $D\emptyset$ experiment has no Roman pots⁸, so that DPE dijet production operationally is defined as two hard jets in the final state which are separated from both sides of the beamline by large rapidity gaps. The dijet cuts are $E_T > 12\text{GeV}$ for $D\emptyset 630$ and $E_T > 15\text{GeV}$ for $D\emptyset 1800$ with $|y_1|, |y_2| < 1.0$ for both center-of-mass energies.

The $D\emptyset$ approach has both an advantage and a disadvantage to the CDF approach. The advantage is $D\emptyset$ implements on-line jet triggering. Thus, they are able to make a more efficient usage of their collected data sample. In addition 12 and 15 GeV jets are much better defined for identification by cone algorithms. The disadvantage of the $D\emptyset$ approach is without Roman pots the same ambiguities experienced by CDF arise here and are magnified. In particular uncertainty remains about what portion of the double gap events are double diffractive, single diffractive/single pomeron exchange or double pomeron exchange. Moreover the momentum fractions lost by the proton and antiproton are not directly measured, so that in principle the experiment places no restriction on them. An upper bound on the momentum fraction lost by the p and \bar{p} can be estimated by examining the maximum energy deposition in the hard event. From this, it can be inferred [45] that $x_{IP/p}, x_{IP/\bar{p}} \lesssim 0.05$. This bound is consistent with the heuristic notion that a pomeron can carry no more than $\sim 5\%$ of the diffractive hadron's momentum. For the $D\emptyset$ cuts used in our calculations, we will use the upper bound $x_{IP/p}, x_{IP/\bar{p}} < x_{IP}^{\max} = 0.05$. The jet E_T requirements imply a minimum energy must be deposited in the hard interaction region, which places a lower bound $x_{IP/p}, x_{IP/\bar{p}} > x_{IP}^{\min}$ given by

$$E_T^{\min} = \sqrt{\frac{x_{IP}^{\min} x_{IP}^{\max} s}{2}}. \quad (18)$$

For convenience, to accommodate both center-of-mass energy cases, we set $x_{IP}^{\min} = 0.001$, since this limit is lower than the values given by Eq. (18).

For DPE dijets at LHC with $\sqrt{s} = 14,000\text{ GeV}$, we use the following cuts. The transverse jet energy will be $E_T > 10\text{GeV}$ with the rapidity region $-1.0 < y_1, y_2 < 1.0$. These cuts represent standard expectations for jets in the hard DPE process. For the momentum

⁸In Run II, which is expected to start in late 2000, $D\emptyset$ plans to have Roman pots on both sides of the beamline to detect both the proton and antiproton [49]

fractions lost by the proton and antiproton, four cases will be considered, LHC-1: $0.002 < x_{IP/p,\bar{p}} < 0.03$, LHC-1': $0.00006 < x_{IP/p,\bar{p}} < 0.03$, LHC-2: $0.002 < x_{IP/p,\bar{p}} < 0.01$, and LHC-2': $0.00006 < x_{IP/p,\bar{p}} < 0.01$. These cuts are estimates of where diffraction should be important. The upper bounds are slightly more conservative than the heuristic limit of 0.05. For the LHC-2 and LHC-2' cuts, where the upper bounds are 0.01, diffraction clearly should be dominant as supported by the ZEUS [50] and H1 [51] experiments. The lower bounds on $x_{IP/p,\bar{p}}$ for LHC-1 and LHC-2 again are suggested by the Zeus and H1 data. The lower bound on $x_{IP/p,\bar{p}}$ for the LHC-1' and LHC-2' cases is based on the minimal energy condition for the hard interaction Eq. (18). Here, the lower limit of $x_{IP/p,\bar{p}} > 0.00006$ accommodates both cases, LHC-1' and LHC-2', since this bound is below x_{IP}^{\min} given by Eq. (18).

A. Summary of the Experimental Cuts

For convenience, below the cuts we use to represent the various experiments are summarized.

CDF: $\sqrt{s} = 1800\text{GeV}$, $E_T > 7\text{GeV}$, $-4.2 < y_1, y_2 < 2.0$, $0.015 < x_{IP/p} < 0.035$ (+rapidity side), $0.04 < x_{IP/\bar{p}} < 0.095$ (-rapidity side).

DØ1800: $\sqrt{s} = 1800\text{GeV}$, $E_T > 15\text{GeV}$, $-1.0 < y_1, y_2 < 1.0$, $0.001 < x_{IP/p}, x_{IP/\bar{p}} < 0.05$

DØ630: $\sqrt{s} = 630\text{GeV}$, $E_T > 12\text{GeV}$, $-1.0 < y_1, y_2 < 1.0$, $0.001 < x_{IP/p}, x_{IP/\bar{p}} < 0.05$

LHC-1: $\sqrt{s} = 14,000\text{GeV}$, $E_T > 10\text{GeV}$, $-1.0 < y_1, y_2 < 1.0$, $0.002 < x_{IP/p}, x_{IP/\bar{p}} < 0.03$

LHC-1': $\sqrt{s} = 14,000\text{GeV}$, $E_T > 10\text{GeV}$, $-1.0 < y_1, y_2 < 1.0$, $0.00006 < x_{IP/p}, x_{IP/\bar{p}} < 0.03$

LHC-2: $\sqrt{s} = 14,000\text{GeV}$, $E_T > 10\text{GeV}$, $-1.0 < y_1, y_2 < 1.0$, $0.002 < x_{IP/p}, x_{IP/\bar{p}} < 0.01$

LHC-2': $\sqrt{s} = 14,000\text{GeV}$, $E_T > 10\text{GeV}$, $-1.0 < y_1, y_2 < 1.0$, $0.00006 < x_{IP/p}, x_{IP/\bar{p}} < 0.01$

IV. RESULTS

In this section, the results of our calculations are presented. Then, various cross-checks and features of the results are discussed. Finally a qualitative comparison is made of our results with the preliminary results from the CDF and DØ experiments.

A. Presentation

Calculations have been performed on the y_+ -spectra, E_T spectra, and total cross sections for the N(L)DPE and F(IS)DPE dijet processes with the CDF, DØ and LHC cuts that were discussed in Sect. III. For comparison, the standard inclusive dijet process, Eq. (10), also has been computed with cuts comparable to the corresponding CDF, DØ and LHC DPE cuts. In particular, the corresponding inclusive dijet cuts we use are for CDF: $\sqrt{s} = 1800\text{GeV}$, $E_T > 7\text{GeV}$, $-4.2 < y_1, y_2 < 2.0$, DØ1800: $\sqrt{s} = 1800\text{GeV}$, $E_T > 15\text{GeV}$, $-1.0 < y_1, y_2 < 1.0$, DØ630: $\sqrt{s} = 630\text{GeV}$, $E_T > 12\text{GeV}$, $-1.0 < y_1, y_2 < 1.0$, and LHC: $\sqrt{s} = 14,000\text{GeV}$, $E_T > 10\text{GeV}$, $-1.0 < y_1, y_2 < 1.0$.

Our results for the y_+ and E_T spectra are presented in Figs. 5 - 8 for respectively CDF, DØ1800, DØ630 and LHC. In all four of these figures, the (a) graphs contains the y_+ -spectra for the N(L)DPE and F(IS)DPE models, the (b) graphs contains the ratio of y_+ spectra

between the DPE and inclusive processes, $(d\sigma_{DPE}/dy_+)/(d\sigma_{incl.}/dy_+)$, the (c) graphs contain the E_T -spectra for the N(L)DPE and F(IS)DPE models and the (d) graphs contain the ratio of the E_T spectra between the DPE and inclusive processes, $(d\sigma_{DPE}/dE_T)/(d\sigma_{incl.}/dE_T)$. In the CDF and DØ figures, the solid curves represent the F(IS)DPE ACTW A-SG models and the dashed curves represent the N(L)DPE model with Sudakov suppression factor Eq. (16) none (i.e. $F_S = 1$) and $\mu^2 = 1.0, 0.3$ GeV 2 . The DØ figures also have dashed-dotted and dotted curves, which represent for the F(IS)DPE and N(L)DPE processes respectively some modified cuts. The specifics of these curves will be explained at the appropriate time in the discussion that follows. For the LHC Fig. (8), the F(IS)DPE ACTW D model is represented for LHC-1,2 by the solid curves and LHC-1',2' by the dashed-dotted curves and the N(L)DPE Sudakov suppressed $\mu^2 = 0.3$ model is represented for LHC-1,2 by the dashed curves and the LHC-1',2' by the dotted curves.

The total cross sections for all the DPE dijet cases are in table 1. For the corresponding inclusive dijet cases, the total cross sections are

$$\begin{aligned}\sigma_{\text{incl}}^{\text{CDF}} &= 1.9 \text{ mb}, \\ \sigma_{\text{incl}}^{\text{DØ1800}} &= 0.023 \text{ mb}, \\ \sigma_{\text{incl}}^{\text{DØ630}} &= 0.013 \text{ mb}, \\ \sigma_{\text{incl}}^{\text{LHC}} &= 0.71 \text{ mb}.\end{aligned}\tag{19}$$

For the F(IS)DPE case, we use the best fit value of the pomeron intercept found by ACTW [36], $\alpha_{IP} = 1.144$. Also, the ACTW pomeron parton distributions were dependent on α_{IP} as a consequence of their fitting procedure, and we have used the ones at $\alpha_{IP} = 1.144$. These distribution functions are evolved with three flavors of quarks. Further details about the ACTW pomeron parton distribution functions can be found in their paper [36]. For the inclusive process, the CTEQ5 parton distribution functions were used [37]. The inclusive distribution functions also were evolved with three quark flavors. Finally in all our calculations, we set $\Lambda_{QCD} = 0.271$ GeV.

B. Discussion and Cross-Checks

This subsection highlights some interesting features of the results and explains their underlying origins. The F(IS)DPE and inclusive cross section formulas for dijet production are well known in the literature. We simply will quote where necessary properties about the various quantities that enter in these expressions such as the parton distribution functions, pomeron flux-factor and hard matrix element. On the other hand, the N(L)DPE dijet cross section formula is less familiar. In [23] it was noted that for forward scattering of both hadrons and with no Sudakov suppression factor, $F_S = 1$, the square of the amplitude Eq. (14) becomes

$$|\overline{\mathcal{M}}(0,0)|^2 = 64\pi \left(\frac{d\sigma(0)}{dt} \right)_{\text{el}} \delta_{ij} \delta_{kl} H_{ijkl},\tag{20}$$

where H_{iijj} is the square of the hard parton amplitude. Its exact expression is given in [23], which evaluates to be $\sum_{ij} H_{iijj} = 18[4\pi\alpha(E_T^2)]^2(N_c^2 - 1)\cosh^4(y_-/2)$. Using these expressions, Eq.(13) crudely can be approximated by the following expression which can be evaluated upon inspection,

$$\frac{d\sigma_{N(L)DPE}^{dijet}}{dE_T^2 dy_1 dy_2} \approx \left(\frac{d\sigma}{dt}\right)_{el} \int_{\perp\text{-region}}^{\text{approximate}} d^2\mathbf{Q}_p d^2\mathbf{Q}_{\bar{p}} \frac{\sum_{ij} H_{iijj}}{2^{10}\pi^6 E_T^4 \cosh^4(y_-/2)} |F_S(\mathbf{0}, E_T^2)|^2, \quad (21)$$

where the Sudakov suppression factor is approximated at the $\mathbf{k} = 0$ point. In this expression, the integral of the two diffractive protons' outgoing transverse momentum phase space ($\mathbf{Q}_p, \mathbf{Q}_{\bar{p}}$) can be approximated as

$$\int_{\perp\text{-region}}^{\text{approximate}} d^2\mathbf{Q}_p d^2\mathbf{Q}_{\bar{p}} \approx \pi^2 |t|_{max}^2, \quad (22)$$

where $|t|_{max}$ is a fixed parameter that represents the characteristic transverse momentum cut-off for the diffractive protons. With these approximations, and $(d\sigma/dt)_{el} = 201\text{mb/GeV}^2$, which is obtained from the optical theorem from the total cross section $\sigma_{tot}^{\bar{p}p} = 62\text{mb}$ [38], Eq. (21) becomes

$$\frac{d\sigma_{N(L)DPE}^{dijet}}{dE_T^2 dy_1 dy_2} \approx (45.8\text{mb/GeV}^2) |t|_{max}^2 \frac{\alpha^2(E_T^2)}{E_T^4}. \quad (23)$$

To determine $|t|_{max}$, the above expression can be compared to the exact numerical expression, Eq. (13), at one point. From this, we will set $|t|_{max} \approx 0.26\text{GeV}^2$.

The three subsections to follow examine the CDF, DØ and LHC cases in turn, with cross checks and explanations offered for the various features of the results in Figs. 5 - 8. One immediate cross check of our results is the magnitudes of the cross sections. For the F(IS)DPE case, we have verified that our results agree with [30]. For the N(L)DPE case⁹, it will be seen below that the exact numerical results are consistent with the approximate expression Eq. (23).

1. CDF

The CDF results in Fig. 5 have the following noteworthy features. From Figs. 5a and 5b, the y_+ -spectra for the N(L)DPE process (dashed curves) are localized to the region $-1 \lesssim y_+ \lesssim 0$. The y_+ -spectra is broader for the F(IS)DPE (solid curves) versus N(L)DPE case, but from Fig. 5b both are less broad than the inclusive y_+ -spectra. Turning to the E_T -spectra, from Fig. 5c the N(L)DPE process falls much slower than the F(IS)DPE process.

⁹The exclusive double diffractive model in [40] has a more detailed description of the two-gluon pomeron process compared to our model. For this reason, direct comparison of total cross sections is not possible between our model and theirs. In the conclusion, we will discuss further the model in [40].

In fact from Fig. 5d, the N(L)DPE process is seen to be almost flat for $E_T < 45\text{GeV}$ for the two cases with Sudakov suppression and slightly rising for the case with no Sudakov suppression. Then for $E_T > 45\text{GeV}$, all three cases rapidly fall to zero. For reference, an exactly flat spectra in Fig. 5d would imply it has the same shape as the inclusive E_T -spectra. Thus the two Sudakov suppressed N(L)DPE E_T -spectra have approximately the same shape as the inclusive E_T -spectra. On the other hand, for the F(IS)DPE spectra, all five cases fall much more rapidly in Fig. 5d relative to the inclusive spectra, with the SG case falling the least rapidly.

The behavior of the CDF N(L)DPE spectra can be understood from the approximate Eq. (23) and by examining the dijet rapidity phase space. Recall for N(L)DPE processes, the parton momentum fractions x_h that enter the hard interaction equal the corresponding pomeron momentum fractions $x_{IP/h}$, $\beta_h = x_h/x_{IP/h} = 1$. As such from Eq. (8), the cuts on $x_{IP/h}$ imply direct restrictions on the jet rapidities y_1, y_2 . One finds upon inspection of Eq. (8) and the explicit CDF rapidity cuts from Sect. III that at $E_T = 7\text{GeV}$, dijets only appear in the rapidity ranges $1.4 \lesssim y_1 \leq 2, -3.3 \lesssim y_2 \lesssim -2.3$ (and interchange $y_1 \longleftrightarrow y_2$), which equivalently implies $-1.4 \lesssim y_+ \lesssim -0.15$. As E_T increases, the kinematically allowed rapidity bands move inwards towards zero rapidity. Generally both bands also get narrower. However, since the rapidity band at the proton side (+rapidity) was prematurely cut-off at 2 due to the explicit rapidity cuts, this band first broadens up to $E_T \sim 14\text{GeV}$ and then narrows thereafter for higher E_T . As such at $E_T = 14(28)\text{GeV}$ dijets appear in the bands $0.5(-0.3) \lesssim y_1 \lesssim 1.5(0.75), -2.6(-1.8) \lesssim y_2 \lesssim -1.5(-0.7)$ (and interchange $y_1 \longleftrightarrow y_2$), which corresponds to $-1.1 \lesssim y_+ \lesssim 0$ at both E_T scales. These considerations suffice to explain the localized y_+ -spectra in Figs. 5a and 5b for the N(L)DPE process.

Applying these estimates to Eq. (23), the differential cross section $d\sigma_{N(L)DPE}/dE_T$ at, for example, $E_T = 7, 14, 28\text{GeV}$ gives the relative magnitudes 1, 0.2, 0.03, which are within a factor 2 of the exact numerical results in Fig. 5c. This figure also indicates that the region above $E_T > 30\text{GeV}$ accounts for less than 0.5% of the total N(L)DPE cross section. A check of the dijet phase space indicates that above this E_T , the accessible region is rapidly diminishing. In fact due to the kinematic constraints, the maximum energy that can be deposited in the hard region for either the F(IS)DPE or N(L)DPE processes is $\sqrt{x_{IP/p}^{\max} x_{IP/\bar{p}}^{\max} s}$ which for the CDF cuts implies the largest dijet E_T is $E_T \lesssim 51\text{GeV}$. For the N(L)DPE case, this cutoff is best seen in Fig. 5d.

The last point to address about the CDF N(L)DPE process is the magnitude of the total cross section. The exact numerical results are given in Table 1. Estimates based on Eq. (23), where the phase space integral and all other quantities are approximated at $E_T = E_T^{\min} = 7\text{GeV}$, agree up to a factor 2 with the results in Table 1, including the ratio amongst the three cases of Sudakov suppression, none, $\mu^2 = 1\text{GeV}^2$, and $\mu^2 = 0.3\text{GeV}^2$, of respectively 1, ~ 0.5 , ~ 0.25 .

Turing to the F(IS)DPE process, the first point to be addressed is the steeper decrease of the E_T -spectra in Figs. 5c and 5d relative to both the N(L)DPE and inclusive E_T -spectra. Two facts are useful for this analysis. First, as E_T increases, in general, the average value of x_p and $x_{\bar{p}}$ increase, since more energy must be deposited into the hard region. Second, the pomeron parton distribution functions $f_{i/PP}(\beta_h)$ at small argument $\beta_h \equiv x_h/x_{IP/h}$ grow as $f_{i/PP}(\beta \rightarrow 0) \sim \beta^{-a}$ with $0 \lesssim a \lesssim 1.5$, and at large argument

vanish as $f_{i/PP}(\beta \rightarrow 1) \sim (1 - \beta)^b$ with $0 \lesssim b \lesssim 1.0$. Thus at small E_T , x_p and $x_{\bar{p}}$, and so therefore also $x_p/x_{PP/p}$ and $x_{\bar{p}}/x_{PP/\bar{p}}$, are closer to their kinematic lower bounds, which implies the parton distribution functions are at their largest. However as E_T increases, it implies $\beta_h = x_h/x_{PP/h} \rightarrow 1$ so that $f_{i/PP}(x_h/x_{PP/h}) \rightarrow 0$. In contrast, within the same E_T range, the behavior of the inclusive parton distribution functions is very different, primarily due to the difference in behavior of their arguments. The inclusive distribution is evaluated with respect to x_h not $x_h/x_{PP/h}$. Since $x_h^{\min} < x_h < x_{PP/h}$ and $x_{PP/h} < 0.1$, x_h within this range always is relatively small. Thus the inclusive parton distributions within the equivalent E_T range have less variation and generally are large. This difference in behavior of the arguments for inclusive and F(IS)DPE parton densities explains the steeper decline of the latter's E_T -spectra relative to the former.

There are two immediate checks that verify the above observations about the E_T -spectra. First pomeron parton distribution functions that fall slower as $\beta \rightarrow 1$ should have flatter E_T -spectra in Fig. 5d and this is the case for the ACTW SG model. Second, if the upper limits on $x_{PP/p, \bar{p}}$ are increased, then for fixed x_h , the ratio $x_h/x_{PP/h}$ is smaller. Thus, for the same jet kinematics, $f_{i/PP}(x_h/x_{PP/h})$ should fall less rapidly, which in turn would flatten the E_T -spectra in Fig. 5d. One can verify this effect for any general pomeron parton distribution function.

To further quantify the above observations about the CDF case, we can ask how small do the the parton momentum fractions become. From Eq. (18), naturally the minimum value for one occurs, when the other is at its maximum. As a more realistic estimate, let us assume the "large" region for the parton momentum fractions is when $x_h/x_{PP/h} \gtrsim 0.5$, since above this point the pomeron parton distribution functions rapidly vanish. Thus the parton carrying the "large" momentum fraction will have $x_{h_{large}} \approx 0.5x_{PP/h_{large}}^{\max}$. We substitute $x_{h_{large}}$ in the LHS of Eq. (18). We now ask above what E_T will the other parton momentum fraction also be in the "large" region, under the assumption that when both parton's momentum fractions are "large", there is negligible contribution to the cross section. By this criteria, we find that both momentum fractions are in the 'large" region, which means $x_p \gtrsim 0.025$ on the proton side and $x_{\bar{p}} \gtrsim 0.03$ on the antiproton side, once $E_T \gtrsim 35\text{GeV}$.

Although for the pomeron case, these momentum fractions are large because $\beta_h \sim 1$, the situation is different for the inclusive case. The inclusive parton distribution functions are evaluated with respect to x_h , not $\beta_h = x_h/x_{PP/h}$. As such the range for their arguments is $x_{p, \bar{p}} \sim 0.02 - 0.04$ and within this range the parton distribution functions have very little variation. The numbers quoted in this example are very crude, but they illustrate the reason in Fig. 5d for the F(IS)DPE E_T spectra's steeper decline relative to the inclusive case.

The above discussion ignored entirely complications from the pomeron flux factor f^{DL} . This is because its approximate behavior is $f^{DL} \sim x_{PP}^{1-2\alpha_{PP}}$ and in either of the two ranges $0.015 < x_{PP/p} < 0.035$ or $0.04 < x_{PP/\bar{p}} < 0.095$, its variation is relatively small, i.e. less than a factor 3.

It is worth noting that the rise in the N(L)DPE E_T spectra in Fig. 5d has similar explanation to the one given above for the differences in E_T -spectra between the F(IS)DPE and inclusive cases. In particular, the inclusive parton distribution functions will fall a little as E_T increases since the average values of x_h will increase. However the proton form factors in our N(L)DPE model are insensitive to this variation. This is one of the primary

differences between the N(L)DPE model and both the inclusive and F(IS)DPE models, and it explains the relative rise in the former's E_T spectra to the latter. Furthermore, the rise is less pronounced for the Sudakov suppressed N(L)DPE processes, since they provide greater suppression to the N(L)DPE differential cross section $d\sigma/dE_T$ as E_T rises.

In the N(L)DPE model, this lack of x_h -dependence in the proton form factors is not a fundamental requirement for nonfactorization of the CFS type. This is a simplying limitation in this particular model. In [40] nonfactorizing models similar to our N(L)DPE model were treated, except with more detailed modeling of the x_h dependences. We will discuss the models in [40] later in the paper, but we will not explore such modification to our model in this paper.

Next, we will understand the behavior of the y_+ -spectra for the F(IS)DPE case in Fig. 5a and 5b. To simplify the problem, we assume the main features of the spectra are determined by the low E_T dijets $E_T \approx E_T^{\min} = 7\text{GeV}$. We want to understand why the y_+ -spectra is broader for the F(IS)DPE versus N(L)DPE case and moreover why the former also is skewed towards the $-y_+$ side. For this, note that at fixed x_p , $x_{\bar{p}}$, and E_T , the largest y_+ attainable by the dijets is when both are on the same side with equal rapidity, $y_- = 0$. In this case Eq. (8) becomes

$$\frac{x_p}{x_{\bar{p}}} = \frac{2E_T}{\sqrt{s}} \exp(\pm y_+). \quad (24)$$

By evaluating $x_{p,\bar{p}}$ within their allowed range, this expression gives the limits on y_+ . The allowed ranges for $x_{p,\bar{p}}$ are determined by the same criteria as before that both momentum fractions must be "small", $x_h/x_{IP/h} < 0.5$. This condition implies the ranges $x_p \lesssim 0.02$, $x_{\bar{p}} \lesssim 0.05$, with the lower limits in both cases governed by the energetic condition Eq. (18). By these crude approximations, the y_+ range for the spectra is $-1.9 \lesssim y_+ \lesssim 1.0$, which coincides reasonably well with the exact numerical results in Fig. 5a. Furthermore, one finds as the boundaries of the y_+ range are approached, x_p and $x_{\bar{p}}$ are increasing for both the inclusive and F(IS)DPE cases. As such, the contributions from the respective parton distribution functions are decreasing. In particular, the distribution functions decrease slower for the inclusive versus F(IS)DPE case, since the range of the argument in the former is much smaller $\lesssim 0.1$ versus the latter $\lesssim 1$. This part of the explanation is the same as our earlier discussion which compared the E_T -spectra for these two processes. The final outcome is the F(IS)DPE y_+ -spectra for all the models in Fig. 5b are narrower than the inclusive one.

The last point to note is that the total cross sections in table I for the five models come in the ratio 1(A):100(B):1(C):400(D):20(SG). To obtain insight into these ratios, it is useful to decompose the cross section in terms of the parton initiated processes. For the B,D and SG models we find $\sim 80\%$ of the cross section comes from the pure gluon process $\hat{\sigma}_{gg}$ and the remaining fraction predominately from the $\hat{\sigma}_{gq}$ process. On the other hand, for the A and C models, the cross section decomposes as less than 5% from $\hat{\sigma}_{gg}$, $\sim 40\%$ from $\hat{\sigma}_{gq}$ and $\sim 60\%$ from the pure quark initiated process $\hat{\sigma}_{qq} + \hat{\sigma}_{\bar{q}q}$. Therefore the B,D, and SG models are more gluon controlled whereas the A and C models are more quark controlled. However, for none of the five models is it the case that one species of partons, quarks or gluons, dominates the cross section.

To cross check these findings, we examine the pomeron parton distribution functions in the most probable β range, which we estimated above to be $\sim 0.01 - 0.1$. Two features

about the parton distribution functions are evident. First, in this β range, the A and C or B and D distributions are the same magnitude, with the latter pair about a factor 10 larger than the former pair and the SG distribution is a factor 3-5 larger than the former. Second, for a given parton model, the ratio of the gluon to quark parton distribution function in this β range, $f_{g/\text{IP}}(\beta)/f_{q/\text{IP}}(\beta)$, is for the A and C models 3 – 20, the B and D models 20 – 50 and the SG model 10 – 30. These properties are consistent with the general trends found amongst the five models for the total cross section. However since this turns out to be an intermediate regime between quarks and gluons, these simple indicators are insufficient to better quantify the results found from the exact numerical calculations.

2. $D\emptyset$

The $D\emptyset 1800$ results in Fig. 6 have the following interesting features. Both the N(L)DPE (dashed curves) and F(IS)DPE (solid curves) y_+ -spectra are localized to the region $|y_+| < 1$. In contrast to the CDF case, here the F(IS)DPE y_+ -spectra is slightly narrower than the N(L)DPE y_+ -spectra, which best is seen in Fig. 6b. For the E_T -spectra, similar to the the CDF case the N(L)DPE process falls with increasing E_T much slower than the F(IS)DPE process. In comparison to the inclusive process, for the N(L)DPE case both the y_+ -spectra in Fig. 6b and E_T spectra for $E_T \lesssim 40\text{GeV}$ in Fig. 6d are flat, thus have the same shape as the corresponding inclusive spectra. On the other hand, for the F(IS)DPE case, the y_+ -spectra in Fig. 6b is much more localized than the inclusive spectra and the E_T -spectra in Fig. 6d falls much faster.

The basic features of the N(L)DPE spectra can be understood, once again, through the approximate cross section formula Eq. (23) and by examining the available dijet rapidity region based on the explicit $D\emptyset$ rapidity cuts and those implied by the cuts on $x_{\text{IP}/p,\bar{p}}$. Carrying out this analysis, at the lowest $E_T = 15\text{GeV}$ we find that the cuts on $x_{\text{IP}/p,\bar{p}}$ place no additional restrictions, so that the available rapidity region is $-1 < y_1, y_2 < 1$. As E_T increases, the first rapidity region that diminishes is for same-side jets and starting at the periphery. The reason is evident from Eq. (8). At fixed $|y_1|$ and $|y_2|$, x_p and $x_{\bar{p}}$ differ more for same-side dijets than for opposite-side dijets. As such, the larger of the two parton momentum fractions will reach its upper limit at smaller y_1 and y_2 for same-side versus opposite-side dijets. For example, the available rapidity region at $E_T = 20(30)\text{GeV}$ for opposite-side jets is unchanged $0 < y_1 < 1$ and $-1 < y_2 < 0$ (and interchange $y_1 \leftrightarrow y_2$) whereas for same-side jets the rapidity regions are $0 < y_1, y_2 < 0.8(0.4)$ and $-0.8(-0.4) < y_1, y_2 < 0$. By $E_T > 30\text{GeV}$ all regions of rapidity space diminish. For example at $E_T = 40\text{GeV}$, the allowed rapidity space is $0 < y_1 \lesssim 0.5$, $-0.5 \lesssim y_2 < 0$ (and $y_1 \leftrightarrow y_2$) and $0 < y_1, y_2 \lesssim 0.2$ and $-0.2 \lesssim y_1, y_2 < 0$. Finally for $E_T \gtrsim 45\text{GeV}$ there is no allowed rapidity region.

Integrating over the rapidity region in Eq. (23) with these estimates, we find consistency with the exact numerical results for $d\sigma(E_T)/dE_T$ in Figs. 6c and 6d. Also the rapid cutoff in the E_T -spectra at $E_T \approx 45\text{GeV}$, best seen in Fig. 6d, is consistent with our crude estimates here that the available rapidity phase space vanishes at this point.

For the N(L)DPE y_+ -spectra in Fig. 6a, we again can apply the above results, except integrating Eq. (23) over E_T and y_- . The basic shape of the y_+ -spectra can be understood

by assuming dominance of the low E_T regime $E_T \sim 15\text{GeV}$ and examining the behavior of the y_- phase space as a function of y_+ . For the latter we find at $y_+ = 0$ the y_- range is $\Delta y_-(y_+ = 0) = 4$ and it vanishes linearly to zero as $y_+ \rightarrow 1$. In fact relative to linear decrease as a function of y_+ , the y_+ -spectra in Figs. 6a and 6b is more enhanced near the middle $y_+ = 0$ relative to the periphery $y_+ = 1$. This is an effect of higher E_T -dijets. Recall from above that as E_T increases, the rapidity region first to diminish is for same-side dijets, or equivalently the large y_+ region. For example at $E_T = 20\text{GeV}$ the region $1 < |y_+| < 0.8$ no longer has dijets. In general higher E_T dijets enhance the region near $y_+ = 0$ relative to $y_+ = 1$.

To estimate the N(L)DPE total cross from the approximate expression Eq. (23), the E_T integral is performed with the rapidity phase space region evaluated at $E_T = 15\text{GeV}$. The latter yields a rapidity area ~ 4 , which implies for no Sudakov suppression the estimate $\sigma \approx 1.7\mu\text{b}$. Evaluating the Sudakov suppression factor at $E_T = 15\text{GeV}$ leads to suppression factors to the total cross section of ~ 0.67 and ~ 0.11 for $\mu^2 = 1\text{GeV}^2$ and $\mu^2 = 0.3\text{GeV}^2$ respectively. These estimates are within a factor 2 of the exact numerical results in table 1.

Turning to the F(IS)DPE process, the steeper E_T -spectra relative to both the N(L)DPE and inclusive processes arises for reasons similar to the CDF case discussed earlier. In particular, the high E_T region in general requires higher parton momentum fractions, which are suppressed by the pomeron parton distribution functions. For $E_T \gtrsim 22\text{GeV}$ both incoming partons to the hard process carry "large" momentum fractions, $x_h/x_{IP/h} > 0.5$. Thus above this E_T , one should expect the E_T spectra to diminish as evident in Figs. 6c and 6d. For example relative to the inclusive E_T -spectra, the F(IS)DPE E_T -spectra decreases for the A,B,C,D, SG models at $E_T = 22\text{GeV}$ by the additional factors 6, 9, 6, 9, 3 respectively and at $E_T = 30\text{GeV}$ by the additional factors 100, 250, 100, 250, 27 respectively. This faster decline for the F(IS)DPE E_T spectra arises because the edge (i.e. $\beta \sim 1$) of the pomeron parton distribution functions is being reached. Consistently, the slowest decline of the E_T -spectra amongst the five models is by the SG model, whose parton distribution function decreases the slowest at $\beta \rightarrow 1$.

For the y_+ -spectra in Figs. 6a and 6b, their shape can be understood through rapidity phase space consideration and the behavior of the pomeron parton distribution functions. Generally larger $|y_+|$ requires larger x_p and $x_{\bar{p}}$. Similar to the N(L)DPE case, at $E_T = 20\text{GeV}$, for example, the $x_{IP/p, \bar{p}}$ and dijet rapidity cuts prohibit dijets for $|y_+| \gtrsim 0.8$. In addition to simple phase space restrictions, for the F(IS)DPE process larger parton momentum fractions x_p and $x_{\bar{p}}$ thus larger $|y_+|$ are further suppressed due to the pomeron parton distribution functions. This additional source of suppression at large $|y_+|$ explains in Figs. 6a and 6b. why the F(IS)DPE y_+ -spectra are a little narrower than the N(L)DPE ones.

Turning to the magnitude of the cross sections, from table 1 the relative sizes amongst the five parton distribution functions are about the same as in the CDF case discussed earlier, $1(A) : 50(B) : 1(C) : 200(D) : 50(SG)$. These ratios can be cross checked with the general behavior of the F(IS)DPE cross section formula, similar to our earlier treatment for the CDF case. Basically one finds that these ratios are consistent with the ratios of the pomeron parton distribution functions in the typical β regime ($\beta \sim 0.1$).

Finally, it is interesting to compare cross section magnitudes between DØ1800 and CDF.

If the DPE dijet process is N(L)DPE dominated, the CDF and DØ1800 cases differ primarily by phase space area and the $1/E_T^2$ scaling factor. Despite the larger CDF central rapidity region, once their $x_{IP/p,\bar{p}}$ cuts are considered, the dijet phase space area between CDF and DØ1800 is approximately the same. As such the predominant difference between the CDF and DØ1800 cross sections is due to the $1/E_T^2$ factor, which if evaluated at their respective minima implies the N(L)DPE cross sections of DØ1800 should be a factor ~ 4 smaller than those of CDF. This is consistent with table 1.

On the other hand, for a F(IS)DPE dominated dijet process, in addition to the above two factors, an additional difference arises from the pomeron parton distribution functions. They make a significant difference due to their rapid growth at small- β . Very roughly, since for CDF E_T^{\min} is a factor 2 smaller and the average x_{IP} is a factor 2 larger compared to DØ1800, the typical β at which the pomeron parton distribution functions are evaluated in the CDF case should be a factor 4 smaller relative to DØ1800. By knowing the typical β range for the two cases, we can estimate the behavior of the parton distribution functions in that range. We expect that within the kinematically accessible range of β , the typical range that dominates the cross section will be near its minimum limit since that is where the parton distribution functions will be the largest. The smallest β possible based on Eq. (18) is 0.015 and 0.11 for CDF and DØ1800 respectively. However at this limit, although one parton distribution function will be large, this effect is compensated by the other parton distribution function, which must be evaluated at $\beta = 1$ where it vanishes. Thus β regions away from this limit also will contribute significantly. As an estimate of an upper bound to the typical β range, we estimate at E_T^{\min} for $x_p = x_{\bar{p}}$ and when x_{IP} is at an average value, which we will take as ~ 0.05 and ~ 0.025 for CDF and DØ1800 respectively. Then we obtain $x_h = 0.0077$ and 0.017 so that $\beta = 0.15$ and 0.70 for CDF and DØ1800 respectively. So in summary the typical β ranges are $0.15 - 0.015$ for CDF and $0.70 - 0.11$ for DØ1800. These estimates confirm that the typical β are a factor $4 - 7$ smaller for the CDF case versus the DØ1800 case. Moreover the size of β for both cuts is $O(10^{-1})$. In this β range, the growth of all five ACTW pomeron parton distribution functions is $\sim 1/\beta^{1.2-1.3}$. Thus the typical size of a pomeron parton distribution function in the CDF case will be a factor $\sim (4 - 7)^{1.2-1.3}$ bigger than the DØ1800 case. Accounting for this factor for each of the two parton distribution functions and the factor 4 from E_T scaling, we expect the cross section for any given pomeron parton distribution function model to be a factor $\sim 10^2$ larger for CDF relative to DØ1800. This essentially is what is found in table 1.

Note that the size of the typical β found above is interesting in its own right. It implies the range of β probed in both the CDF and DØ1800 cases is not tiny. Recall that very tiny β is the natural regime for gluon dominance. Thus, for the CDF and DØ1800 cuts, one should not assume that gluon dominance is necessary and we have shown earlier by explicit examples that there are parton distribution functions models (A and C in particular) in which that assumption is wrong.

For DØ630, the qualitative features of the spectra basically are the same as for DØ-1800. In Fig. 7a, the y_+ -spectra for the N(L)DPE process is a little broader compared to the F(IS)DPE process. For both the F(IS)DPE and N(L)DPE processes the y_+ -spectra is contained in a much smaller region, $|y_+| \lesssim 0.3$, compared to DØ1800. However, similar to DØ1800, the E_T -spectra for the N(L)DPE case falls much slower than for the F(IS)DPE case.

From Fig. 7d, the relative decline of N(L)DPE E_T -spectra to the inclusive case is faster than in the DØ1800 case. More noticeably, in comparison to DØ1800, the F(IS)DPE E_T -spectra falls much faster relative to the corresponding inclusive E_T -spectra. In particular, the ratio of the F(IS)DPE to the inclusive E_T -spectra for DØ630 falls by two orders of magnitude within an increase of E_T by 2GeV whereas for the DØ1800 case the same decrease requires an increase of E_T by 15GeV.

To understand the features of the N(L)DPE case from Eq. (23), first note that at $E_T = 12(15)\text{GeV}$ the allowed rapidity region for opposite-side dijets is $0 < y_1 < 0.75(0.40)$, $-0.75(-0.40) < y_2 < 0$ (and $y_1 \leftrightarrow y_2$) and same-side dijets is $0 < y_1, y_2 < 0.25(0.10)$, $-0.25(-0.10) < y_1, y_2 < 0$. By $E_T \geq 18\text{GeV}$ there is no accessible jet rapidity region. As such the explicit jet rapidity cuts of $|y_i| < 1$ are irrelevant since the upper bounds $x_{IP/p, \bar{p}} < 0.05$ already prohibit sufficient energy deposition to produce dijets at the higher $|y_i|$ region at even the lowest permissible E_T . These crude estimates along with Eq. (23) show consistency with the exact numerical results in Fig. 7 and table 1. Finally since the jet rapidity region is rapidly shrinking even at the lowest E_T , this explains the more rapid decline of of the E_T -spectra between the N(L)DPE and inclusive processes for this case compared to DØ1800. This effect can be reversed by increasing the upper limit on $x_{IP/p, \bar{p}}$. For example, the dotted curves in Figs. 7a-d present the various N(L)DPE spectra for Sudakov suppression with $\mu^2 = 0.3$ and when $x_{IP/p}, x_{IP/\bar{p}} \leq 0.1$

For the F(IS)DPE process, the explanation for the two spectra essentially is the same as in the DØ1800 case. The important quantitative difference is the typical parton momentum fractions are much bigger here than for DØ1800. This explains the sharper fall of both the y_+ and E_T -spectra. For example, to produce 12GeV dijets with the minimal energy deposition, so at $y_- = 0$, requires for symmetric parton momentum fractions $x_p = x_{\bar{p}} = 0.038$. Thus almost all the DØ630 events are in the “large” β regime, $\beta_h \equiv x_h/x_{IP/h} \gtrsim 0.5$. Recall in this region the pomeron parton distribution functions are rapidly diminishing. As such, the sharp decline in the E_T -spectra for DØ630 relative to the inclusive case primarily is because the periphery of the parton distribution functions at $\beta \sim 1$ are being probed. This sharp decline can be reduced if the limits on $x_{IP/p}$ and $x_{IP/\bar{p}}$ are increased. For example, the dashed-dotted curves in Figs. 7a-d present the various F(IS)DPE spectra for the ACTW model D when $x_{IP/p}, x_{IP/\bar{p}} \leq 0.1$

3. LHC

The LHC results in Fig. 8 have the following interesting features. In Figs. 8a and 8b, the y_+ -spectra for the N(L)DPE LHC-1 and LHC-2 cases (dashed curves) are much narrower than for all the other cases. Relative to the inclusive y_+ -spectra in Fig. 8b, all the F(IS)DPE cases and the N(L)DPE LHC-1' and LHC-2' cases (dotted curves) are flat, whereas the N(L)DPE LHC-1 and LHC-2 cases drop-off as $|y_+|$ increases with the latter falling fastest. For the E_T -spectra in Fig. 8c, the most intersting feature is for the N(L)DPE LHC-1 and LHC-2 cases, for which the E_T -spectra actually first rises with increasing E_T until $E_T \approx 15\text{GeV}$ and thereafter falls. In contrast for N(L)DPE LHC-1' and LHC-2', the E_T -spectra are of a more standard behavior. For the F(IS)DPE E_T -spectra, the LHC-2 (solid curves) and LHC-2' (dashed-dotted curves) cases fall much faster with increasing E_T

than the LHC-1 (solid curves) and LHC-1' (dashed-dotted curves) cases. In fact, in Fig. 8d the F(IS)DPE LHC-1 and LHC-1' E_T spectra are almost as flat as the N(L)DPE LHC-1' and LHC-2' cases.

For the N(L)DPE case, the primary difference between the primed and unprimed spectra arise due to the different lower bounds on $x_{IP/p,\bar{p}}$ of 0.00006 and 0.002 respectively. Due to the high \sqrt{s} relative to the CDF and DØ cases studied earlier, much smaller parton momentum fractions are necessary to produce kinematically identical dijets. In fact the larger lower cut-off in $x_{IP/p,\bar{p}}$ for the LHC-1 and LHC-2 cases already is too large to produce substantial numbers of dijets in the range $10\text{GeV} < E_T \lesssim 15\text{GeV}$. For example, the only rapidity region where $E_T \approx 10\text{GeV}$ dijets can appear is for opposite-side jets with $0.6 < y_1 < 1$, $-1.0 < y_2 \lesssim -0.6$ (and $y_1 \leftrightarrow y_2$). Once E_T rises to 15GeV , the same-side jet region becomes accessible starting with the region $y_1 \approx y_2 \approx 0$ and moving outward to higher rapidity with increasing E_T . This behavior also explains the narrower y_+ -spectra for the N(L)DPE LHC-1 and LHC-2 cases in Figs. 8a and 8b. In the dominant E_T range $10\text{GeV} < E_T \lesssim 15\text{GeV}$, dijets predominately emerge within ~ 0.2 y_+ -rapidity units about $y_+ = 0$. The shoulder of the y_+ -spectra in Fig. 8a at $y_+ \sim 0.4$ corresponds to $E_T \sim 20\text{GeV}$.

In contrast, for the LHC-1' and LHC-2' cuts, the lower limit on $x_{IP/p,\bar{p}}$ imposes no constraints on jet rapidity. In this case, starting at $E_T = 10\text{GeV}$, the complete rapidity region $-1 < y_1, y_2 < 1$ is accessible. The explanation for the y_+ and E_T spectra in this case follows similar reasoning to the DØ1800 cases discussed earlier.

To compare the magnitude of the N(L)DPE cross sections in table 1 with Eq. (23), the dijet phase space must be estimated. For the N(L)DPE LHC-1' and LHC-2' cases at $E_T = E_T^{\min} = 10\text{GeV}$ the entire explicit rapidity region $-1 < y_1, y_2 < 1$ is accessible with no additional constraints from the x_{IP} cuts. This obtains the estimate with no Sudakov suppression of $\sigma \approx 4\mu\text{b}$. For the N(L)DPE LHC-1 and LHC-2 cases, because of the the large lower limit on x_{IP} , at $E_T = 10\text{GeV}$ dijets only appear in a small region of opposite-side dijet rapidity space with $\Delta y_+ \Delta y_- \approx 0.3$. However at $E_T \approx 15\text{GeV}$, the entire opposite-side jet rapidity region is accessible $0 < y_1 < -1$, $-1 < y_2 < 0$ (and $y_1 \leftrightarrow y_2$) but as yet only a negligible region of same-side jet rapidity space. Thus the total rapidity area is $\Delta y_+ \Delta y_- \approx 2$. Observe that the gain in phase space area is a factor 3 greater than the suppression factor of 9/4 from the $1/E_T^2$ behavior of σ . This is consistent with the rise in the E_T -spectra in Fig. 8a. Applying the above estimates to Eq. (23) implies for no Sudakov suppression $\sigma \approx 1\mu\text{b}$. The Sudakov suppression factor evaluated at $E_T = 10\text{GeV}$ implies the cross section in both cases should decrease by factors 0.4 for $\mu^2 = 1\text{GeV}^2$ and 0.2 for $\mu^2 = 0.3\text{GeV}^2$. These crude estimates are consistent with the exact numerical results in table 1.

For the y_+ F(IS)DPE spectra in Fig. 8b, they are very similar to their inclusive counterparts. This contrasts the CDF and DØ cases in Figs. 5b, 6b, and 7b. The reason is the higher \sqrt{s} , which for fixed E_T and y_+ , requires smaller parton momentum fractions $x_{p,\bar{p}}$. Assuming the shape of the y_+ -spectra is dominated by the lowest $E_T \approx 10\text{GeV}$ region, for the full range of $|y_+| < 1$, $\beta_i \equiv x_h/x_{IP/h}$ typically never is "large" $\beta_i < 0.5$. Thus for the full y_+ range the pomeron parton distribution functions typically are not probed near $\beta \rightarrow 1$ where they vanish. Instead, they typically are probed at intermediate β regions, similar to the situation in the corresponding inclusive case. This is the basic reason for the similarity in the y_+ -spectra between the F(IS)DPE and inclusive processes.

For the F(IS)DPE E_T -spectra from Fig. 8d the flatness of the LHC-1 and LHC-1' cases again arises from the small typical β values at which the pomeron parton distribution functions are evaluated. The sharper decrease of the F(IS)DPE LHC-2 and LHC-2' cases arises due to the lower upper bounds on $x_{IP/p,\bar{p}}$ of 0.01, versus 0.03, for the LHC-2 and LHC-2' cases. The main consequence of these different upper bounds appears in the parton distribution functions and not from phase space. This is evident since only the latter effect is relevant for the N(L)DPE cases, and for them the E_T -spectra at large E_T has no pronounced difference in all 4 cases. On the other hand, for the pomeron parton distribution functions, the two different upper bounds on $x_{IP/p,\bar{p}}$ imply that for fixed E_T , they are probed in the LHC-2 and LHC-2' cases at typical β values that roughly are 3 times larger relative to the LHC-1 and LHC-1' cases. This factor 3 difference has nonnegligible effect. Noting that the order of magnitude of the typical x_h is $> O(10^{-3})$ or equivalently $\beta_h > 0.06$, with this lower bound increasing with E_T , the factor 3 means the difference between β close to 0.1 where the parton distribution functions are sizable and β closer to 1 where they vanish rapidly.

C. Comparison with Experiment

Both CDF [31,32,43,44,52] and DØ [45–48] have reported preliminary results on the double diffractive dijet process. In Sect. III limitations of both experiments were discussed which prohibit explicit measurement of the DPE dijet process in the present runs. Nevertheless, one likely possibility considered by both experiments is that the majority of the double diffractive dijet events were DPE. Under this assumption, some of the reported features from these experiments will be interpreted below in terms of the models examined in this paper.

DØ reports its E_T -spectra for the DPE dijet process to be similar to the inclusive E_T -spectra with comparable cuts [45–48]. The earlier CDF preliminary reports [31,32,43,44] also found this, although their most recent report [52] finds the E_T -spectra falls much faster than for the comparable inclusive E_T -spectra. Based on Figs. 5d, 6d, 7d, 8d, the DØ and earlier CDF E_T -spectra lean towards that for the N(L)DPE process. Amongst the F(IS)DPE processes, the E_T -spectra for the best fit ACTW model, D, as well as model B differ significantly from their inclusive counterpart. However they could be consistent with the most recent CDF report [52]. The F(IS)DPE model with the most similar E_T -spectra to the inclusive process, is ACTW SG. Recall in this model the gluon density peaks near $\beta = 1$.

In the DØ case, as noted earlier, by increasing the upper bounds on $x_{IP/p}$ and $x_{IP/\bar{p}}$, the E_T spectra could be more flattened in Figs 6d and 7d. In Figs. 6 and 7, the various spectra with upper bounds $x_{IP/p}, x_{IP/\bar{p}} \leq 0.1$ are shown as the dotted curves for the N(L)DPE case with Sudakov suppression at $\mu^2 = 0.3$ and the dashed-dotted curves for the F(IS)DPE ACTW D model. Observe the dashed-dotted curves in Figs. 6d and 7d for the ACTW D model are significantly flatter than any of the F(IS)DPE cases with upper bounds $x_{IP/p,\bar{p}} < 0.05$ (solid curves) (for comparison, the dotted curves in these figures are for the N(L)DPE model with $\mu^2 = 0.3$ and $x_{IP/p,\bar{p}} < 0.1$). Since DØ does not explicitly measure $x_{IP/p,\bar{p}}$, one explanation for their E_T -spectra is the F(IS)DPE model with the higher upper limits on $x_{IP/p,\bar{p}}$, say between 0.05 – 0.1. In such a case, recall that the interpretation of pomeron dominated exchange enters into question. For DØ1800 larger upper limits on $x_{IP/p,\bar{p}}$ are inconsistent with the largest DPE dijet E_T that is found, ~ 52 GeV. This maximum is consistent with

an upper bound of only $x_{IP/p,\bar{p}} < 0.057$. On the other hand, for DØ630, note from [45,48] that dijets are produced up to $E_T \sim 25$ GeV. If background and resolution effects or any other experimental complication can be ruled out, this suggests for DØ630 $x_{IP/p,\bar{p}} \lesssim 0.08$.

For the y_+ -spectra, the CDF results unambiguously contradict interpretation as N(L)DPE dominated. The CDF y_+ -spectra is very broad, ranging as $-2 \lesssim y_+ \lesssim 1.5$. From Fig. 5a, this is similar to the F(IS)DPE cases and is completely at odds with the N(L)DPE cases. Recall for the CDF cuts, the narrower y_+ -spectra for the N(L)DPE model is intrinsic to its lossless nature. Thus the experimental y_+ -spectra is strong indication that the F(IS)DPE process dominates in the CDF case. This interpretation also is consistent for the E_T -spectra in the most recent CDF report [52]. However, for the E_T -spectra from the earlier CDF reports [31,32,43,44], ACTW SG is the most consistent model. Finally, one can not exclude the possibility that the N(L)DPE process gives a nondominant but measurable effect. This would help flatten any of the F(IS)DPE models in Fig. 5d. However an admixture of the N(L)DPE process also will imply greater enhancement of the y_+ -spectra in the region $-1 \lesssim y_+ \lesssim 0$.

Finally, total cross sections can be compared. CDF has preliminarily reported a DPE dijet cross section of $\sigma_{DPE}^{CDF} \approx 13.6$ nb [31]. DO has given no preliminary cross section, although for DØ1800 they have estimated $\sigma_{DPE}^{DØ} \sim 10$ pb [46]. In this case, the CDF total cross section is about 1000 times larger than DØ1800. The model that most closely obtains this factor difference is F(IS)DPE ACTW D, which predicts the ratio to be still a factor 5 smaller. As another case, for ACTW SG, it predicts the CDF total cross section should be only a factor ~ 50 larger than DØ1800. Furthermore, the predicted ratio between the CDF and DØ1800 total cross sections decreases if the limits on $x_{IP/p,\bar{p}}$ for DØ1800 are increased. Thus there appears to be some discrepancy between the experimental cross sections and those predicted by all the F(IS)DPE models. Also, the N(L)DPE models do very poorly in predicting the observed ratio. For the largest ratio predicted by these models, the CDF total cross section would be only a factor 7 larger than DØ1800. However for the N(L)DPE case, modifications of the proton form factor and two-gluon pomeron model, which are discussed in the conclusion, may change these predictions by an order of magnitude but not more.

V. CONCLUSION

The emerging picture found here is the preliminary CDF and DØ DPE dijet data favor domination by the F(IS)DPE process. From comparison of our models with the CDF preliminary data, the mean rapidity spectra provide the most suggestive evidence that the data is dominated by the F(IS)DPE process. However there remain inconsistencies with this conclusion. In particular, the harder E_T -spectra for DØ and the earlier CDF results do not agree with the best fit ACTW F(IS)DPE model. Also, the experimental ratio of the CDF to DØ1800 total cross sections is a factor 5 – 10 larger than predicted by any of the models examined here. Finally, for the N(L)DPE process, neither data nor our analysis is sufficiently precise to rule out a subdominant component. These are important issues to resolve as further experimental data becomes available. For the time being, the limitations of both the CDF and DØ experiments for this process exclude any final conclusions to be drawn.

Our study emphasized the hard physics, but made minimal attempt at modeling most of the nonperturbative soft physics. For example, general belief is hard, pure hadron induced, diffractive processes are subject to a weakly \sqrt{s} -dependent suppression factor [33,53], which represents the probability for the rapidity gap(s) not to be filled by extra exchanges of pomerons and gluons between the particles in the model which have very different rapidities. Such absorptive corrections potentially can be treated by the methods developed in [33]. In [40], they used the approach of [33] and [54] to estimate the absorptive correction factor for the DPE dijet process and at $\sqrt{s} = 1800$ GeV found it to be ~ 0.06 . For our calculations, this factor is meant to multiply the results in Table 1.

For the N(L)DPE model, also not treated here is modifications of the two gluon exchange model with LLA ladder evolution of gluons. A model for this was given in [40]. Their model amounts to including in the N(L)DPE dijet amplitude two factors of gluon densities evaluated at $x_{IP/p}$ and $x_{IP/\bar{p}}$. This modification has interesting consequences. For example, maintaining the same procedure to normalize the DPE dijet amplitude with respect to the elastic $p\bar{p}$ cross section, the N(L)DPE cross section with this modification then will be 1 – 2 orders of magnitude smaller. This arises because the normalization constant is fixed for elastic scattering process, where $x_{IP/p,\bar{p}}^{\text{elastic}} \sim 1_\perp/\sqrt{s}$ is small since 1_\perp , the transverse momentum of the outgoing hadrons, is ~ 1 GeV. For example at $\sqrt{s} = 1800$ GeV, $x_{IP/p,\bar{p}}^{\text{elastic}} \sim 0.0006$. On the other hand, for the N(L)DPE process the typical $x_{IP/p,\bar{p}}$ are ~ 0.01 . These are much larger, which implies a relative decrease of the gluon densities. This provides an additional suppression compared to the same model with no gluon densities. In [40], the exclusive double diffractive dijet model is the same as our N(L)DPE model here, except for the inclusion of gluon densities in their model. It is due to the effect of these densities that their model predicts cross sections 1 – 2 orders of magnitude smaller than ours.

Another effect of the gluon densities is the N(L)DPE E_T -spectra will fall faster with E_T . The reasons for this are the same as explained in Sect. IV for the F(IS)DPE models. In short, higher E_T requires larger $x_{IP/p,\bar{p}}$ which in turn implies smaller gluon densities. This effect will be less pronounced for the N(L)DPE models versus the F(IS)DPE models, since the argument of the gluon densities in the former always remain small, $\lesssim x_{IP}^{\text{max}} \sim 0.1$ whereas in the latter it ranges up to ~ 1 , where the maximum diminution of the gluon densities occurs.

In summary, this paper examined two very different types of diffractive mechanisms for DPE dijet production, the factorized Ingelman-Schlein and nonfactorized lossless mechanisms. In the spirit of Regge physics, both mechanisms were termed double pomeron exchange. Some of the differences between the two processes have been elucidated here, which will help in interpreting experiment. The F(IS)DPE model appears best to represent the present experimental data. However, inconsistencies still remain that need to be sorted-out by both theory and experiment before final conclusions can be made. Although the N(L)DPE process does not appear to dominate the cross section, a subdominant component of it can not be excluded with present information. The cleanliness of the final state in this process, two outgoing hadrons plus a hard event, suffices justification to search for it. For new particle search experiments, this process could permit the ultimate measurement, although its diminutive cross section precludes it from being the ideal measurement. Thus as should be the case with any good tale, the hard double pomeron exchange story is filled with uncertainties and conflicts. Furthermore, the hope vested in the N(L)DPE process

someday may vindicate a familiar moral, that the best things don't come easy.

ACKNOWLEDGMENTS

I thank the following for helpful discussions: L. Alvero, J. Collins, M. Strikman, J. Whitmore, R. Hirosky, T. Taylor-Thomas, M. Albrow, K. Goulianos, P. Melese, and K. Terashi. I also thank L. Alvero for use of his pomeron parton distribution codes and for contributions to the earlier developments of this paper. This work was supported in part by the U.S. Department of Energy.

REFERENCES

- [1] G. Alberi and G. Goggi, Phys. Rept. **74**, 1 (1981).
- [2] K. Goulianos, Phys. Rept. **101**, 169 (1983).
- [3] UA4 collaboration, M. Bozzo *et al.*, Phys. Lett. B **155** (1985) 197; Phys. Lett. B **171** (1986) 142.
- [4] G. Ingelman and P.E. Schlein, Phys. Lett. **B152**, 256 (1985).
- [5] H. Fritzsch and K. K. Streng, Phys. Lett. **B164**, 391 (1985); K. H. Streng, Phys. Lett. **B166**, 443 (1986); K. H. Streng, Phys. Lett. **B171**, 313 (1986).
- [6] E.L. Berger, J.C. Collins, D.E. Soper and G. Sterman, Nucl. Phys. **B286**, 704 (1987).
- [7] UA8 Collaboration, R. Bonino *et al.*, Phys. Lett. **B211**, 239 (1988).
- [8] UA8 Collaboration, A. Brandt *et al.*, Phys. Lett. **B297**, 417 (1992).
- [9] D. Joyce *et al.*, Phys. Rev. **D48**, 1943 (1993).
- [10] V. N. Gribov, Zh. Eksp. Teor. Fiz. **41**, 1962 (1961); V. N. Gribov and I. Ya. Pomeranchuk Phys. Lett. **9**, 269, (1964).
- [11] T. Regge, Nuovo Cim. **14**, 951 (1959).
- [12] F. E. Low, Phys. Rev. D **12** (1975) 163; S. Nussinov, Phys. Rev. Lett. **34** (1975) 1286; Phys. Rev. D **14** (1976) 246.
- [13] J. F. Gunion and D. E. Soper, Phys. Rev. **D15** (1977) 2617.
- [14] J.C. Collins, D.E. Soper and G. Sterman, “Factorization of Hard Processes in QCD” in “Perturbative QCD” (A.H. Mueller, ed.) (World Scientific, Singapore, 1989).
- [15] A. Berera and D.E. Soper, Phys. Rev. **D50**, 4328 (1994).
- [16] A. Berera and D.E. Soper, Phys. Rev. **D53**, 6162 (1996).
- [17] J.C. Collins, Phys. Rev. **D57**, 3051 (1998).
- [18] L. Trentadue and G. Veneziano, Phys. Lett. **B323**, 201 (1994); M. Grazzini, L. Trentadue and G. Veneziano, Nucl. Phys. **B519**, 394 (1998).
- [19] J.C. Collins, L. Frankfurt and M. Strikman, Phys. Lett. **B307**, 161 (1993).
- [20] L. Frankfurt and M. Strikman, Phys. Rev. Lett. **63** (1989) 1914.
- [21] J. C. Collins, D. E. Soper, and G. Sterman, Nucl. Phys. **B261** (1985) 104; **B308** (1988) 833; G. Bodwin, Phys. Rev. D **31** (1985) 2616; **34** (1986) 3932.
- [22] J. Pumplin, Phys. Rev. **D52** (1995) 1477.
- [23] A. Berera and J.C. Collins, Nucl. Phys. **B474**, 183 (1996).
- [24] A. Bialas and P. V. Landshoff, Phys. Lett. **B256** (1991) 540.
- [25] A. Bialas and W. Szeremeta, Phys. Lett. **B296**, 191 (1992).
- [26] F. Hautmann, Z. Kunszt, and D. E. Soper, Phys. Rev. Lett. **81**, 3333 (1998); hep-ph/9906284.
- [27] A. Hebecker, Nucl. Phys. **B585**, 349 (1997).
- [28] K. Goulianos, Phys. Lett. **B358**, 379 (1995).
- [29] P.V. Landshoff and J. C. Polkinghorne, Nucl. Phys. **B33**, 221 (1971); **B36**, 642 (1972); F. Henyey and R. Savit, Phys. Lett. **B52**, 71 (1974); J. L. Cardy and G. A. Winbow, *ibid* **B52**, 95 (1974); C. DeTar, S. D. Ellis, and P. V. Landshoff, Nucl. Phys. **B87**, 176 (1975).
- [30] L. Alvero, J.C. Collins and J.J. Whitmore, hep-ph/9806340.
- [31] M. G. Albrow, CDF Collaboration, Fermilab-Conf-98/138-E “Di-jet Production by Dou-

ble Pomeron Exchange in CDF”, contribution to LISHEP 98, Rio de Janeiro, February 1998.

[32] K. Goulianos, CDF Collaboration, Proceedings of the XXXIIInd Rencontre de Moriond, “QCD '97 and High Energy Hadronic Interactions”, ed. J. Tran Thanh Van (Editions Frontieres), p. 447.

[33] E. Gotsman, E. M. Levin, and U. Maor, Phys. Lett. **B309**, 199 (1993); **353**, 526 (1995).

[34] E. Eichten, I Hinchliffe, K. Lane, and C. Quigg, Rev. Mod. Phys. **56**, 579 (1984); **58**, 1065 (1986).

[35] A. Donnachie and P. V. Landshoff, Nucl. Phys. **B191**, 309 (1987); **B303**, 634 (1988).

[36] L. Alvero, J.C. Collins, J. Terron and J.J. Whitmore, Phys. Rev. **D59**, 074022 (1999).

[37] H. L. Lai *et. al.*, CTEQ Collaboration, MSU-HEP-903100 hep-ph/9903282, 1999.

[38] A. Donnachie and P. Landshoff, Nucl. Phys. **B231** (1984) 189; Nucl. Phys. **B244** (1984) 322.

[39] A. Berera, “Factorization and Nonfactorization in Diffractive Hard Scattering”, contribution to DIS '97, Chicago, IL, April 1997, hep-ph/9707499.

[40] A.D. Martin, M.G. Ryskin and V.A. Khoze, Phys. Rev. **D56**, 5867 (1997).

[41] V.V. Sudakov, Sov. Phys. JETP **3**, 65 (1956).

[42] J.C. Collins, Phys. Rev. **D22**, 1478 (1980).

[43] P. Melese, CDF collaboration, “Diffractive Dijet Search with Roman Pots at CDF” Report No. Fermilab-Conf-96/231-E.

[44] K. Terashi, CDF collaboration, “Observation of Dijet Production in Double Pomeron Exchange in $\bar{p}p$ Collisions at $\sqrt{s} = 1800\text{GeV}$ ”, contribution to Small x Meeting, Fermilab, IL, 1998.

[45] R. Hirosky, DØ collaboration, “Jet Production with Two Rapidity Gaps”, contribution to LISHEP 98, Rio de Janeiro, February 1998.

[46] K. Mauritz, DØ Collaboration, “Hard Diffraction at DØ”, contribution to Small x Meeting, Argonne, IL, September 1996.

[47] G. Alyes, DØ Collaboration, “Jet Production with Two Rapidity Gaps” contribution to Small x Meeting, Fermilab, IL, September 1998.

[48] K. Mauritz, DØ Collaboration, “Hard Diffraction at DØ”, contribution to DIS '99, Zeuthen, Germany, April 1999.

[49] A. Brandt, DØ Collaboration, “DØ Run II Possibilities”, presented at Physics at Run II Workshop, Fermilab, March 1999.

[50] ZEUS Collaboration, M. Derrick *et al.*, Z. Phys. C **68**, 569 (1995); ZEUS Collaboration, M. Derrick *et al.*, *ibid* **70**, 391 (1996).

[51] H1 Collaboration, C. Adloff *et. al.*, Z. Phys. C **76**, 613 (1997).

[52] K. Terashi, private communication; M. G. Albrow, CDF Collaboration, talk presented at low x physics workshop, Tel Aviv, June 1999.

[53] J.D. Bjorken, Phys. Rev. **D47**, 101 (1993).

[54] A. Rostovtsev and M. G. Ryskin, Phys. Lett. **B390**, 375 (1997).

cuts	$\sigma_{F(IS)DPE}^{dijet}(\mu b)$					$\sigma_{N(L)DPE}^{dijet}(\mu b)$			
	ACTW A	ACTW B	ACTW C	ACTW D	ACTW SG	No Sudakov Suppression	Sudakov Suppression $\mu^2 = 1.0$	Sudakov Suppression $\mu^2 = 0.3$	
CDF	0.011	1.0	0.011	4.2	0.24	5.6	2.5	1.7	
DØ630	2.6×10^{-8}	7.5×10^{-7}	2.9×10^{-8}	2.9×10^{-6}	1.4×10^{-5}	0.19	0.075	0.051	
DØ1800	9.5×10^{-5}	5.2×10^{-3}	9.9×10^{-5}	2.2×10^{-2}	5.4×10^{-3}	1.5	0.37	0.25	
LHC-1	0.027	2.6	0.025	11	0.42	1.6	0.37	0.25	
LHC-1'	0.028	2.7	0.027	11	0.49	5.1	1.8	1.2	
LHC-2	0.0068	0.59	0.0068	2.4	0.15	1.4	0.35	0.23	
LHC-2'	0.0075	0.64	0.0075	2.6	0.19	5.0	1.7	1.2	

Table 1: Double Pomeron Exchange (DPE) dijet total cross sections for the nonfactorized (N) and factorized (F) models.

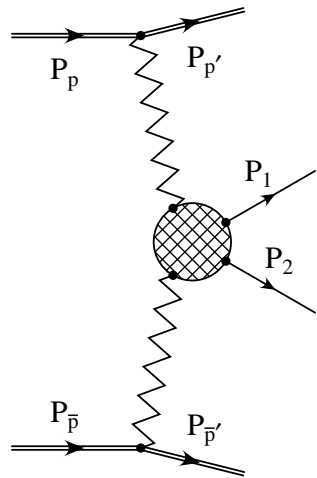


FIG. 1. Double pomeron exchange (DPE) to two jets.

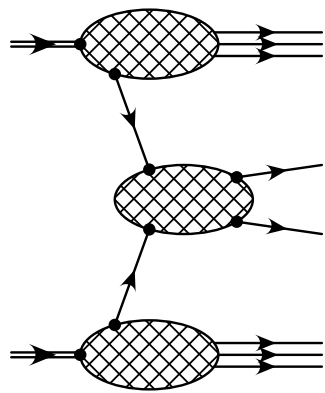


FIG. 2. Amplitude for inclusive two-jet production.

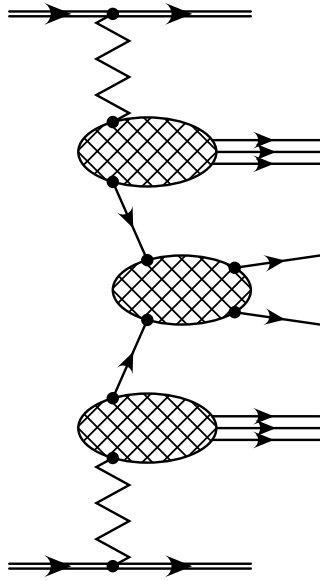


FIG. 3. Factorized (Ingelman-Schlein) Double Pomeron Exchange (F(IS)DPE) amplitude with two jets produced.

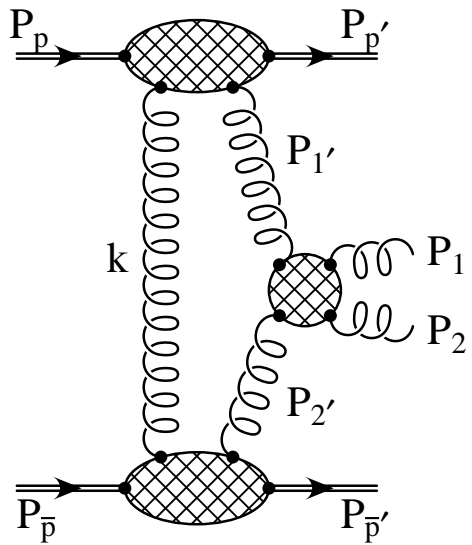


FIG. 4. Our model of the Nonfactorizing (Lossless) Double Pomeron Exchange (N(L)DPE) amplitude with two gluon jets produced.

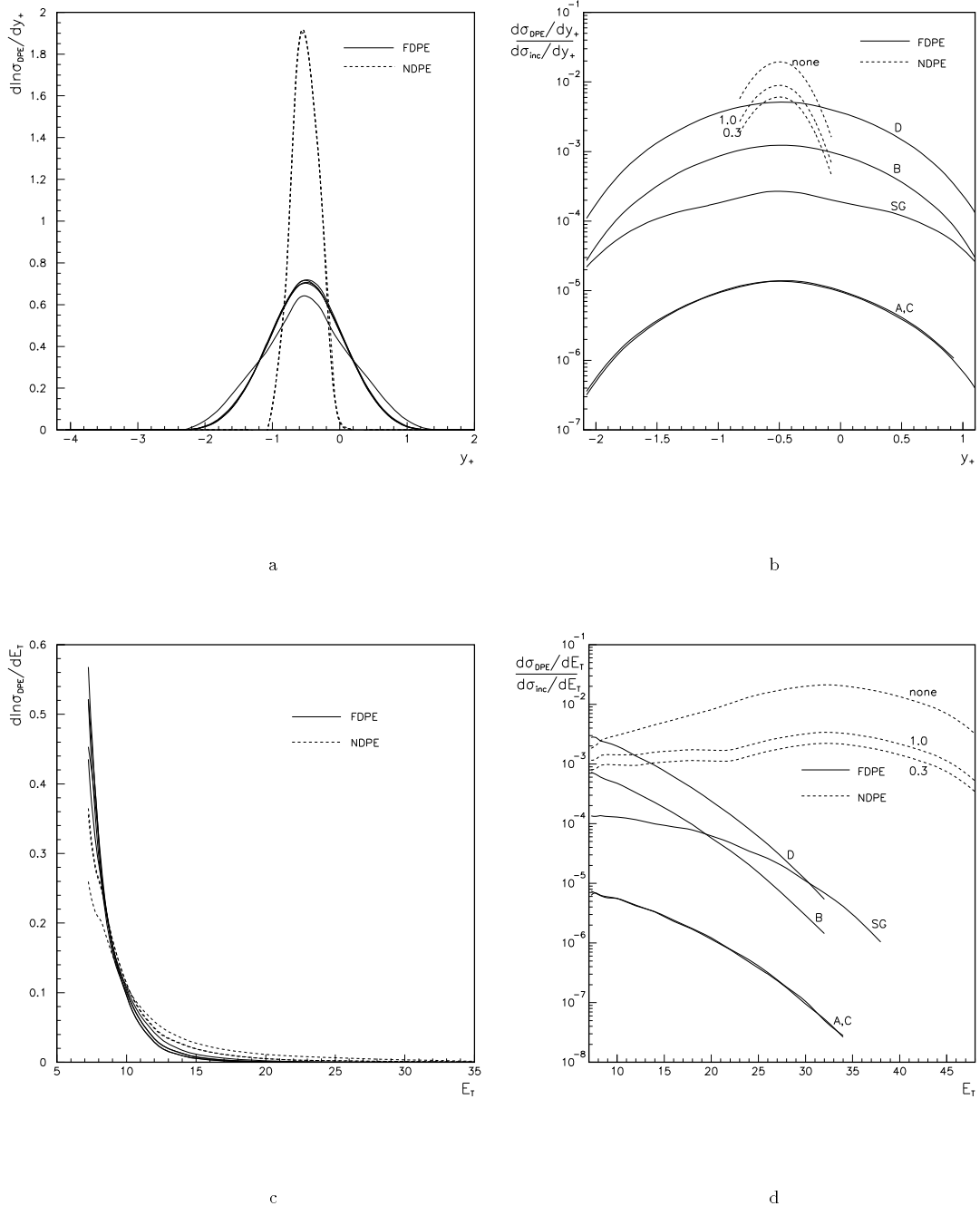


FIG. 5. Double pomeron exchange (DPE) dijet production-CDF cuts. (a) Mean rapidity spectra $y_+ \equiv (y_1 + y_2)/2$. (b) Ratio of mean rapidity spectra between the DPE and corresponding inclusive dijet processes. (c) E_T Spectra. (d) Ratio of E_T Spectra between the DPE and

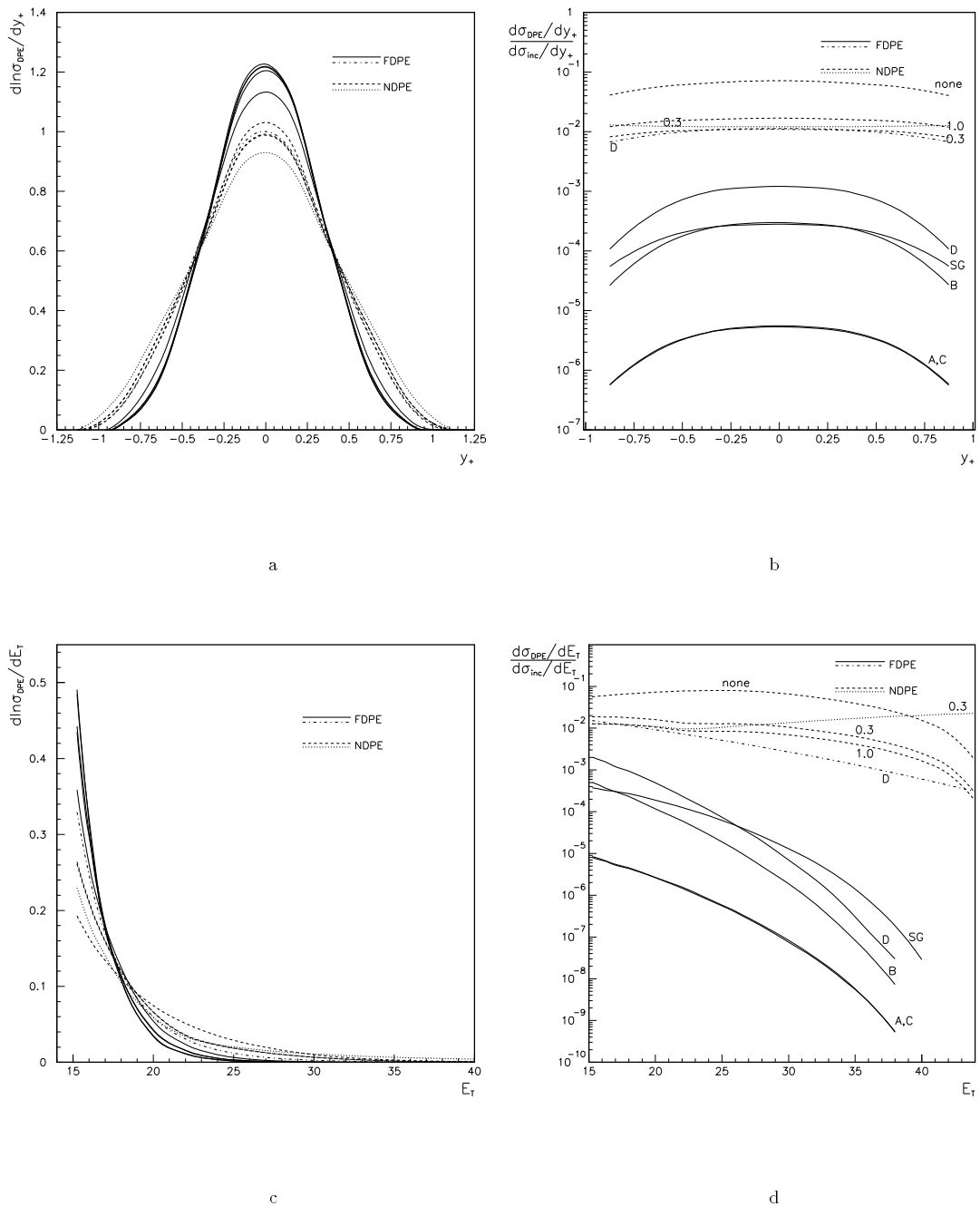


FIG. 6. Double pomeron exchange (DPE) dijet production - DØ1800 cuts. (a) Mean rapidity spectra $y_+ \equiv (y_1 + y_2)/2$. (b) Ratio of mean rapidity spectra between the DPE and corresponding inclusive dijet processes. (c) E_T Spectra. (d) Ratio of E_T Spectra between the DPE and

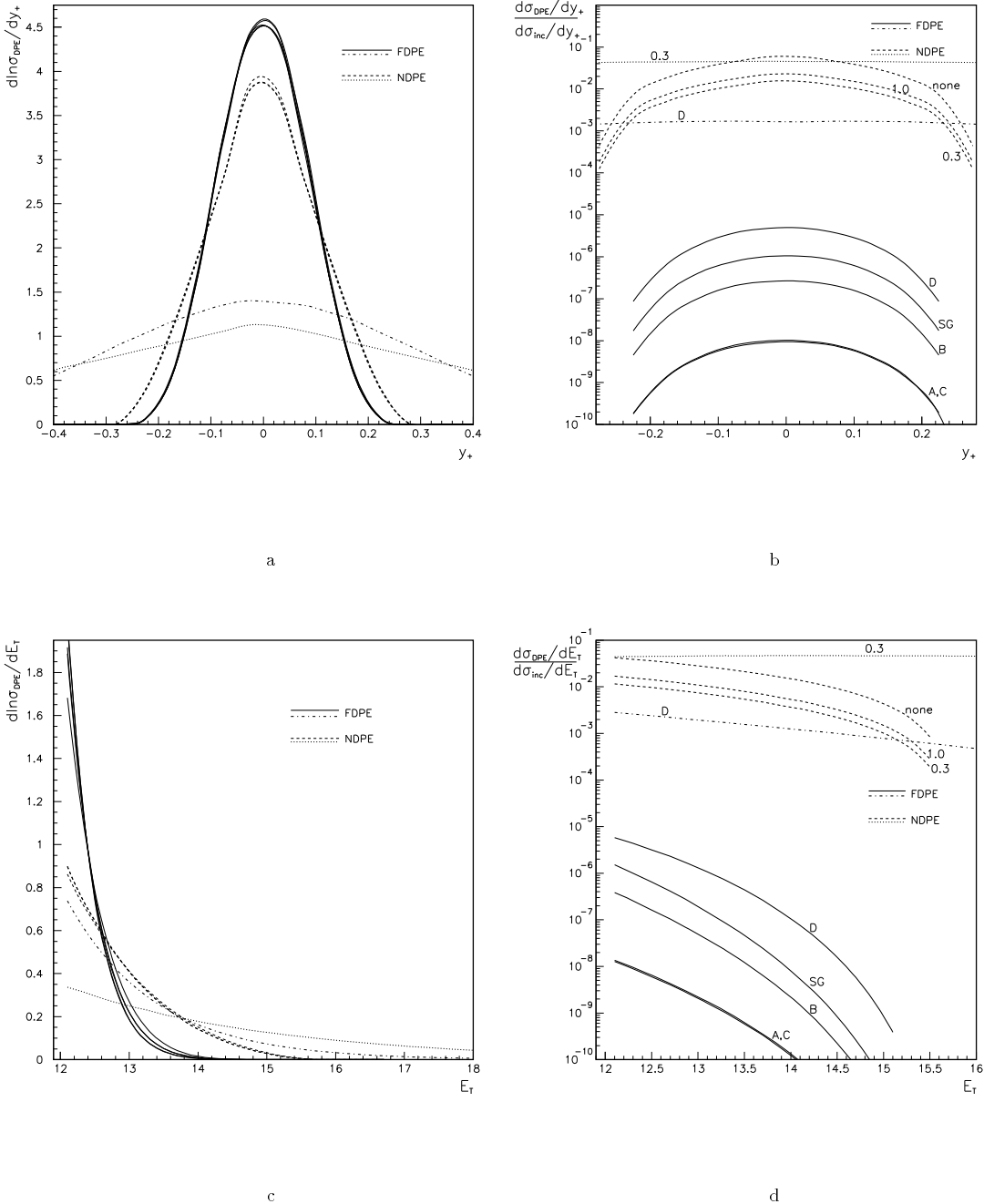


FIG. 7. Double pomeron exchange (DPE) dijet production - D \bar{D} 630 cuts. (a) Mean rapidity spectra $y_+ \equiv (y_1 + y_2)/2$. (b) Ratio of mean rapidity spectra between the DPE and corresponding inclusive dijet processes. (c) E_T Spectra. (d) Ratio of E_T Spectra between the DPE and

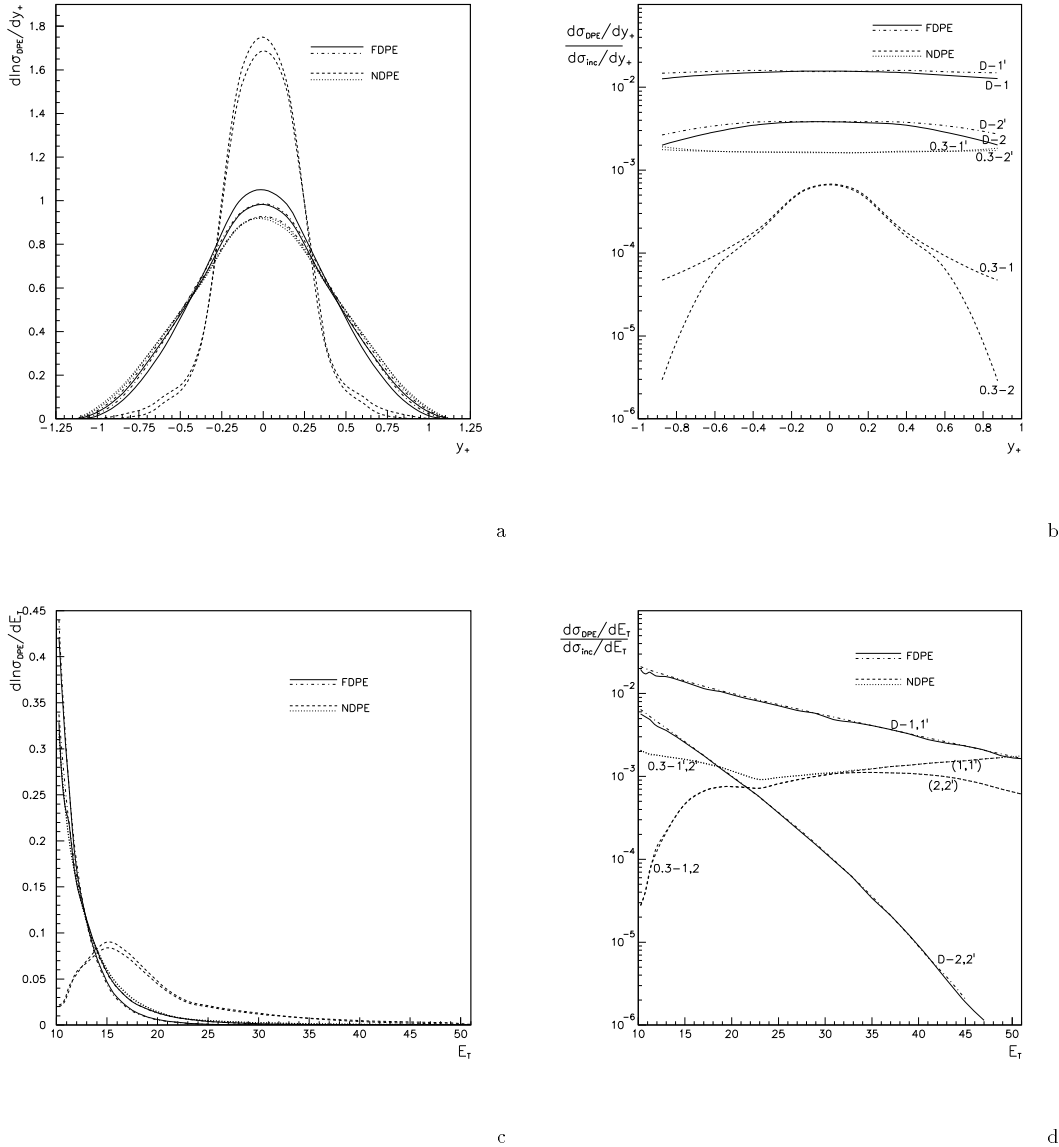


FIG. 8. Double pomeron exchange (DPE) dijet production - LHC cuts. (a) Mean rapidity spectra $y_+ \equiv (y_1 + y_2)/2$. (b) Ratio of mean rapidity spectra between the DPE and corresponding inclusive dijet processes. (c) E_T Spectra. (d) Ratio of E_T Spectra between the DPE and